Eur. Phys. J. A (2023) 59:95
https://doi.org/10.1140/epja/s10050-023-00999-5

THE EUROPEAN PHYSICAL JOURNAL A

Regular Article -Theoretical Physics

Modewise Johnson–Lindenstrauss embeddings for nuclear many-body theory

A. Zare[1,a], **R. Wirth**[2,b], **C. A. Haselby**[3,c], **H. Hergert**[2,4,d], **M. Iwen**[1,3,e]

[1] Department of Computational Mathematics, Science and Engineering, Michigan State University, East Lansing, MI 48824, USA
[2] Facility for Rare Isotope Beams, Michigan State University, East Lansing, MI 48824, USA
[3] Department of Mathematics, Michigan State University, East Lansing, MI 48824, USA
[4] Department of Physics and Astronomy, Michigan State University, East Lansing, MI 48824, USA

Received: 7 November 2022 / Accepted: 6 April 2023

Communicated by V. Somá

Abstract In the present work, we initiate a program that explores modewise Johnson–Lindenstrauss embeddings (JLEs) as a tool to reduce the computational cost and memory requirements of (nuclear) many-body methods. These embeddings are randomized projections of high-dimensional data tensors onto low-dimensional subspaces that preserve structural features like norms and inner products. An appealing feature of randomized embedding techniques is that they allow for the oblivious and incremental compression of large tensors, e.g., the nuclear Hamiltonian or wave functions amplitudes, into significantly smaller random sketches that still allow for the accurate calculation of ground-state energies and other observables. In particular, the oblivious nature of randomized JLE techniques makes it possible to compress a tensor without knowing in advance exactly what observables one might want to approximate at a later time. This opens the door for the use of tensors that are much too large to store in memory, e.g., untruncated three-nucleon forces in current approaches, or complete two- plus three-nucleon Hamiltonians in large, symmetry-unrestricted bases. Such compressed Hamiltonians can be stored and used later on with relative ease. As a first step, we perform a detailed analysis of a JLE's impact on the second-order Many-Body Perturbation Theory (MBPT) corrections for nuclear ground-state observables like the energy and the radius, noting that these will be the dominant corrections in a well-behaved perturbative expansion, and highly important implicit contributions even in nonperturbative approaches. Numerical experiments for a wide range of closed-shell nuclei, model spaces and state-of-the-art nuclear interactions demonstrate the validity and potential of the proposed approach: We can compress nuclear Hamiltonians hundred- to thousandfold while only incurring mean relative errors of 1% or less in ground-state observables. Importantly, we show that JLEs capture the relevant physical information contained in the highly structured Hamiltonian tensor despite their random characteristics. In addition to the significant storage savings, the achieved compressions imply multiple order-of-magnitude reductions in computational effort when the compressed Hamiltonians are used in higher-order MBPT or nonperturbative many-body methods.

1 Introduction

The quantum many-body problem is a prime example of a data-intensive problem with relevance in the fundamental and applied sciences. The structure and dynamics of quantum many-body systems are governed by the stationary and time-dependent Schrödinger equations, respectively. In numerical simulations, they can be cast in the form of matrix eigenvalue or differential equations in straightforward fashion, but the dimension of the involved matrices grows exponentially with the number of particles and their degrees of freedom.

Nowadays, exact diagonalization methods for atomic nuclei like the (No-Core) Shell Model (NCSM) or (No-Core) Full Configuration Interaction (NCFC) [1,2] can tackle dimensions on the order of 10 billion because the natural scales and symmetries of the interactions induce a high degree of sparsity in the involved matrices [3,4]. Still, the memory requirements and computational cost

[a] e-mail: zareali@msu.edu
[b] e-mail: wirth@frib.msu.edu
[c] e-mail: haselbyc@msu.edu
[d] e-mail: hergert@frib.msu.edu (corresponding author)
[e] e-mail: iwenmark@msu.edu

Published online: 02 May 2023

can only be met by supercomputers, and the numerically tractable dimensions are merely sufficient to obtain results for nuclei up to mass $\sim$ 20 in this way, excluding thousands of isotopes that are predicted to exist in nature—many of which will be produced for the first time under laboratory conditions by rare-isotope facilities like the recently launched Facility for Rare Isotope Beams (FRIB) [5].

To overcome the "curse of dimensionality" that plagues exact diagonalization approaches, one can deploy methods that solve the Schrödinger equation with systematic approximations [4], e.g., Many-Body Perturbation Theory (MBPT) based on mean-field wave functions, or sophisticated nonperturbative approaches like the In-Medium Similarity Renormalization Group (IMSRG) [6–8], Coupled Cluster (CC) theory [9,10], or Self-Consistent Green's Function Methods [11–13]. These methods typically scale polynomially with the dimension N of the single-particle basis that defines the degrees of freedom for individual nucleons, and only indirectly with the particle number. For example, the IMSRG at the commonly used IMSRG(2) truncation level naively scales as $O(N^6)$, whereas the more precise next-level truncation IMSRG(3) requires $O(N^9)$ effort.

While greatly extending the range of tractable nuclei [4,14,15], approximate many-body methods become highly data intensive themselves as we strive for greater precision or add degrees of freedom to the single-particle basis. Both efforts are necessary as applications seek to describe exotic nuclei that exhibit deformation and weak-binding effects. They can result in ten- to hundredfold increases in N, which in turn increase the memory requirements and computational cost of many-body calculations by several orders of magnitude, rendering them infeasible with current and next-generation computing resources.

To some extent, the need for large basis dimensions is driven by competing requirements of common many-body frameworks. The two- and three-nucleon interactions that govern nuclear structure and dynamics have compact representations in terms of the relative coordinates, momenta, and spins of the interacting particles, but we can only formulate many-body wave function bases in terms of these degrees of freedom in very light nuclei [16–18]). For mass numbers $A \gtrsim 5$, the computational effort for constructing such wave functions becomes unfeasibly large. Instead, we adopt a formulation based on independent-particle states, the so-called Slater determinants. They are easy to construct because they are simple antisymmetrized products of single-particle wave functions, but not attuned to the description of the correlations that are induced by nuclear interactions. Consequently, an exponentially large basis of Slater determinants is required to capture those correlations. Since interactions still only involve two or three nucleons, this implies a high degree of redundancy in the matrix representations of the interaction operators because the remaining "spectator" nucleons can be in exponentially many configurations. Approximate many-body methods like CC and IMSRG are efficient because they explicitly address part of this redundancy, but they also eventually run out of steam.

To tackle the redundancy problem, one can attempt to identify the principal components of the interactions and wave functions, and leverage the resulting factorizations to change the computational scaling of the targeted many-body methods. In quantum chemistry, for example, efforts to construct factorized CC methods have come to fruition in recent years [19–25], and the adoption of a tensorial viewpoint that better reflects the product nature of the many-body wave functions has proven particularly useful. Similar efforts have been launched in nuclear physics [26–29], but they face their own particular challenges: While nuclei have simpler geometries than molecules, the two- and three-nucleon interactions have a much more complex structure than the Coulomb interaction governing atomic and molecular systems.

A less ambitious approach is to attempt a reduction of the single-particle basis size through an optimization of the orbitals, so that the relevant physics can be captured with fewer degrees of freedom. The design of such optimized basis sets has a long and successful history in quantum chemistry—see for a recent review [30]. In nuclear physics, it is much less common: There is a strong preference for using a basis of (spherical) harmonic oscillator states at least initially because it allows an exact separation of the center-of-mass and relative degrees of freedom in few- and many-body states, provided the basis is truncated appropriately (see, e.g., the discussion in [6] and references therein).

Recent works have demonstrated that the eigenstates of the one-body density matrix with perturbative corrections through second order greatly accelerate the convergence of NCSM/NCFC, IMSRG and CC calculations [31–33]. This implies that the relevant physical information contained in the nuclear Hamiltonian can be compressed from the original working basis into a much smaller natural orbital basis with controllable accuracy.

In the present work, we explore an alternative compression approach that is based on the seminal work of Johnson and Lindenstrauss. Their famous lemma [34] proves that random projections of high-dimensional data into lower dimensional subspaces will preserve structures of the data set like distances and inner products with a high likelihood. Since its publication, it has become an important ingredient for algorithms and data analysis workflows because it mitigates the exponential growth of data sets [35–39].

Modern data science and machine learning have embraced tensorial representations of data for their efficiency, and many of the standard methods and algorithms for data analysis have been extended to tensors as a result [40]. This includes the development of so-called modewise JL embeddings (JLEs) [41] that are the focus of this work. As mentioned above, tensor-based methods are a natural match for the product structure of the many-body Hilbert space and they allow for computation and memory-efficient implementations of standard operations. In essence, modewise embeddings compress the range for the indices of the individual modes of a tensor. In our applications, this corresponds to a reduction of the single-particle basis size from N to cN, where $c < 1$ is a compression factor. Thus, the modewise embeddings are characterized by small matrices of size $O(cN^2)$ that are easy to store, and they can be readily used to embed additional tensors, e.g., for other observables of interest, in a compatible format in future applications.

In the following, we will apply modewise JLEs to the evaluation of nuclear ground-state observables like the binding energy and mean-square radius in Many-Body Perturbation Theory. Our main goal is to develop a detailed understanding of the JLE's impact on second-order MBPT, or MBPT(2), which aims to capture leading-order correlations beyond the mean field (i.e., independent particle) description of atomic nuclei. In a well-behaved MBPT expansion, MBPT(2) will give the dominant corrections to nuclear observables, so this analysis is an important foundation for future applications of the JLE to higher-order MBPT as well as non-perturbative resummation methods.

The implementation of the canonical MBPT(2) requires an $O(N^5)$ single-particle basis change from the working basis in which the interactions are initially prepared to the variationally optimized Hartree-Fock (HF) basis for a particular nucleus [9]. In this basis, the ground-state energy correction can then be implemented with $O(N_o^2 N_u^2)$ computational effort and storage cost, where $N_o \ll N$ and $N_u = N - N_o$ are the number of occupied and unoccupied single-particle states, respectively. Here, we will demonstrate that the modewise JLEs allow us to construct compressed versions of the *full* Hamiltonian, so called random sketches, that are competitive in size with these "minimal" requirements while only incurring a small but controllable loss of accuracy for the MBPT energy and wave function. Although the JLEs do not rely on any prior assumption about the structure of the Hamiltonian at all, they are still able to capture the most relevant physical information. Moreover, the compressed Hamiltonian can be readily stored and used as input for future applications, e.g., in higher-order MBPT or nonperturbative methods. Since the computational scaling of these approaches will be modified from $O(N^k)$ to $O(c^k N^k)$, even modest compressions of the Hamiltonian will also enable order-of-magnitude savings in computational effort.

The computational cost associated with the use of JLEs consists of an additional $O(cN^5)$ basis compression per sample JLE, and the potential evaluation of multiple such samples. Importantly, we will see that the number of samples can be kept small, so that the efficiency gains from the compression are not negated. Although the estimates that a random JLE will yield are themselves random, they are also tightly concentrated around their expectation in distribution, as we will demonstrate explicitly below. Indeed, such "concentration of measure" phenomena are entirely expected and the basis of theoretical proofs of JLE accuracy [34,42,43]. In other words, high errors are exceedingly unlikely even if we only use a single random JLE in the most extreme case.

The scheme we use in the present work is just one particular example for how JLEs can be inserted into nuclear many-body calculations. Indeed, we could readily combine the transformation to the HF basis with the JLE into a single matrix of size $O(cN^2)$ for another modest efficiency gain. Since the JL lemma only relies on the high dimensionality of the data and does not require any assumptions about specific nuclei we are targeting, we will explore whether we can apply the compression earlier in our workflow, perhaps even in the construction of the input interaction tensors. For instance, three-nucleon forces are represented by mode-six tensors and require $O(N^6)$ storage, and even the $O(N^4)$ storage cost for a two-body operator may be prohibitive for large, symmetry-unrestricted single-particle bases, as mentioned earlier.

A second important direction for future work is the design of JLE schemes that are not completely "oblivious" but incorporate some level of physics information, e.g., by importance sampling the underlying random variables. In that case, we will have to carefully assess how the guarantees of the JL lemma may be impacted. We will point out a potential launching point for such studies later in this article.

This work is organized as follows: In Sect. 2, we will briefly discuss the basic ingredients of modewise JLEs. Section 3 reviews the MBPT formalism, with special emphasis on the use of normal-ordered operators and a brief discussion of expectation values for general observables. In Sect. 4, we reformulate MBPT corrections in terms of inner products and derive the expressions for applying one- and two-stage JL embeddings. Numerical results from applications in closed-shell nuclei are analyzed in depth in Sect. 5, and we conclude with a summary and outlook at the next stage of JL applications in Sect. 6. For complete-

ness, we compile numerical results for additional nuclei in Appendix A.

2 Johnson–Lindenstrauss embeddings

2.1 Tensor preliminaries

We detail some terminology and notation that will be useful in describing tensor operations used throughout this work.

The *order* of a tensor is the number of its dimensions or *modes*. That is, $X \in \mathbb{R}^{n_1 \times \ldots n_d}$ is an order d tensor, or a d-mode tensor.

Mode-j fibers are the tensor analogue of rows and columns in the matrix case. They are vectors defined by fixing all but one of the indices and varying the j-th coordinate. For example, tensor $X \in \mathbb{R}^{n_1 \times n_2 \times n_3}$ will have columns, rows and tubes, or mode-1,-2,-3 fibers denoted $\mathbf{x}_{i:k}, \mathbf{x}_{:jk}, \mathbf{x}_{ij:}$ where $i \in [n_1]$, $j \in [n_2]$, $k \in [n_3]$.[1]

The *mode-j unfolding* of a tensor X is a reordering of its elements so that it forms a matrix and is denoted $\mathbf{X}_{(j)}$. It is formed by arranging the mode-j fibers as the columns of the matrix and thus has dimension $n_j \times \prod_{\substack{k=1 \\ k \neq j}}^{d} n_k$. The ordering of these columns is not important so long as it is consistent across calculations. Throughout we use the mapping where tensor entry $(i_1, i_2, \ldots, i_j, \ldots, i_d)$ is identified with matrix element (i_j, J_j) in the mode-j unfolding where,

$$J_j = 1 + \sum_{\substack{k=1 \\ k \neq j}}^{d} (i_k - 1) \prod_{\substack{\ell=1 \\ \ell \neq j}}^{k-1} n_\ell. \tag{1}$$

The *inner product* of two tensors X and Y in terms of their components is

$$\langle X, Y \rangle \equiv \sum_{j_1 \ldots j_d} X_{j_1 \ldots j_d} \overline{Y_{j_1 \ldots j_d}}, \tag{2}$$

where the overline indicates complex conjugation. Note that the set of all d-mode tensors $X \in \mathbb{C}^{n_1 \times \cdots \times n_d}$ forms a vector space over the field of complex numbers when equipped with component-wise addition and scalar multiplication. Further, equipping this vector space with an inner product operation leads to a standard inner product space of tensors and provides a norm $\|X\| = \sqrt{\langle X, X \rangle}$.

2.2 Low-rank tensors

In this section, a brief introduction to low-rank tensors as well as the dimension reduction of tensors using JLEs is presented.

[1] We will use the notation $[n] \equiv \{1, \ldots, n\}$ throughout the paper.

2.2.1 CANDECOMP/PARAFAC decomposition

The Canonical Polyadic Decomposition, also known as CANDECOMP or PARAFAC, and abbreviated here as CPD, decomposes a tensor X into a (weighted) sum of rank-1 tensors [40]. For $X \in \mathbb{R}^{n_1 \times \ldots \times n_d}$,

$$X \approx \hat{X} = \sum_{k=1}^{r} g_k \, \mathbf{v}_k^{(1)} \circ \mathbf{v}_k^{(2)} \circ \cdots \circ \mathbf{v}_k^{(d)}, \tag{3}$$

where $\circ$ denotes the outer product. The vector $\mathbf{v}_k^{(j)} \in \mathbb{R}^{n_j}$ can be considered as the k^{th} column in a matrix $\mathbf{V}^{(j)} \in \mathbb{R}^{n_j \times r}$ for $j \in [d]$. When solving for $\mathbf{V}^{(j)}$ using a CPD fitting algorithm, the columns do not necessarily have unit norms, and so the columns can be normalized and the norms can be stored as weights $g_k = \prod_{j=1}^{d} \|\mathbf{v}_k^{(j)}\|_2$. However, if this normalization is not done, one can assume that all coefficients g_k are one.

2.2.2 Tensor rank

The *rank* of a tensor X is defined as the smallest number of rank-1 tensors that generate X as their sum. In other words, it is the smallest number of components in an *exact* CPD. In the context of Eq. (3), the rank r of a tensor X is defined as the minimum rank r such that $X = \hat{X}$ holds.

Although the definition of tensor rank is analogous to matrix rank, the properties of the two ranks are very different from each other. A major difference is that computation of the rank of a tensor is known to be NP-complete [44]. Therefore, in practice, it is determined numerically by fitting various CP models.

2.3 Johnson–Lindenstrauss embeddings for tensor dimension reduction

Johnson–Lindenstrauss embeddings provide a simple yet powerful tool for dimension reduction of high-dimensional data using random linear projections. The following definition and lemma for matrices (2-mode tensors) is the fundamental building block used to extend results about random projections to tensors of any number of modes with low-rank structure.

Definition 1 A matrix $\mathbf{A} \in \mathbb{C}^{m \times n}$ is an ϵ-JL embedding of a set $S \subset \mathbb{C}^n$ into $\mathbb{C}^m$ if

$$\|\mathbf{A}\mathbf{x}\|_2^2 = (1 + \epsilon_{\mathbf{x}}) \, \|\mathbf{x}\|_2^2, \tag{4}$$

with $|\epsilon_{\mathbf{x}}| \leq \epsilon$ for all $\mathbf{x} \in S$.

Assuming that the elements of $\mathbf{A}$ are independent subgaussian random variables with mean zero and variance m^{-1} and that $|S| = M$, then Eq. (4) holds for all $\mathbf{x} \in S$ with probability $p \geq 1 - 2\exp\left(-Cm\epsilon^2\right)$ if $m \geq C\epsilon^{-2} \log M$, where C is an absolute constant [45].

Lemma 1 *Suppose that* $X, Y \in \mathbb{R}^{n_1 \times \cdots \times n_d}$ *are rank-r tensors of the form*

$$X = \sum_{k=1}^{r} \alpha_k \, \mathbf{v}_k^{(1)} \circ \mathbf{v}_k^{(2)} \circ \cdots \circ \mathbf{v}_k^{(d)}, \tag{5}$$

and

$$Y = \sum_{k=1}^{r} \beta_k \, \mathbf{v}_k^{(1)} \circ \mathbf{v}_k^{(2)} \circ \cdots \circ \mathbf{v}_k^{(d)}. \tag{6}$$

Let $\epsilon \in (0, 3/4]$, *and* $\mathbf{A}^{(j)} \in \mathbb{R}^{m_j \times n_j}$ *be a* $(\epsilon/(4d))$*-JL embedding for each* $j \in [d]$. *Then,*

$$\left| \left\langle X \bigtimes_{j=1}^{d} \mathbf{A}^{(j)}, \; Y \bigtimes_{j=1}^{d} \mathbf{A}^{(j)} \right\rangle - \langle X, \; Y \rangle \right| \leq C \max \left\{ \|X\|^2, \|Y\|^2 \right\}, \tag{7}$$

where C *depends on* ε, r, d *and properties of the space spanned by* $\mathbf{v}_k^{(1)} \circ \mathbf{v}_k^{(2)} \circ \cdots \circ \mathbf{v}_k^{(d)}$. *The complete version of this lemma can be found in Corollary* 1 *in* [41].

In Eq. (7), $X \times_j \mathbf{A}^{(j)}$ denotes the *mode-j product* between X and $\mathbf{A}^{(j)}$. The component-wise definition is,

$$\left(X \times_j \mathbf{A}^{(j)} \right)_{i_1 \ldots i_{j-1} \ell i_{j+1} \ldots i_d} = \sum_{i_j=1}^{n_j} \mathbf{A}^{(j)}_{\ell i_j} X_{i_1 \ldots i_j \ldots i_d}, \tag{8}$$

for $\ell \in [m_j]$ and $i_j \in [n_j]$. In other words Eq. (8) defines the action of contracting the mode-j fibers of X with the rows of matrix $\mathbf{A}^{(j)}$. A useful alternative view of the mode-j product is to recast it as a matrix product between $\mathbf{A}^{(j)}$ and the corresponding mode-j unfolding of the tensor X. That is, $\left(X \times_j \mathbf{A}^{(j)} \right)_{(j)} = \mathbf{A}^{(j)} \mathbf{X}_{(j)}$.

Extending the same idea to multiple modes, the components of the fully projected tensor can be calculated using

$$\left(X \bigtimes_{j=1}^{d} \mathbf{A}^{(j)} \right)_{\ell_1 \ldots \ell_d} = \sum_{i_1=1}^{n_1} \cdots \sum_{i_d=1}^{n_d} X_{i_1 \ldots i_d} \mathbf{A}^{(j)}_{\ell_1 i_1} \cdots \mathbf{A}^{(d)}_{\ell_d i_d}, \tag{9}$$

for $\ell_j \in [m_j]$ and all $j \in [d]$. By applying JL embeddings to a low-rank d-mode tensor X, the size of all modes can be reduced to yield a projected tensor of much smaller size (a so-called random sketch), without the need to reshape the tensor into a single large vector.[2] It is expected then that the Euclidean norm of the projected tensor as well as the inner product between any two tensors lying on the same low-rank subspace are preserved to within predictable errors. Working modewise as per Lemma 1 requires the storage of several small JL matrices, whereas vectorizing the tensor and then using a single matrix to embed it requires significantly more memory since the JL matrix has more entries than the original tensor itself.

[2] For information on mode-j fibers and unfoldings, and mode products in tensors, see [40].

3 Many-body perturbation theory

In the present work, we use the framework of Many-Body Perturbation Theory as a test-bed for the application of JLEs to nuclear interactions and observables. Specifically, we will focus on second-order Møller-Plesset MBPT corrections to the energies and general observables as one of the simplest post-Hartree Fock approaches to capture correlations—deploying the JLEs in nonperturbative techniques like the IMSRG [6,7] or the CC method [9,10] is more challenging, and will be considered in future work.

3.1 Choice of reference state and normal ordering

The starting point for MBPT is the choice of the reference state on which the perturbative expansion will be built. As in any expansion method, this choice will affect both the form and the convergence of the expansion, as discussed in Refs. [46–48], for example. Here, we follow the *canonical* approach and select a Hartree-Fock Slater determinant that has been variationally optimized for a nucleus of interest as our reference. We will denote this state by $|\Phi\rangle$ in the following. This allows us to construct a complete basis for our many-body Hilbert space from all physically allowed excitations of $|\Phi\rangle$.

The Hamiltonian and other observables will be expressed in terms of Fermionic creation ($a_p^\dagger$) and annihilation (a_p) operators that satisfy the fundamental anticommutation relations

$$\left\{ a_p, a_q^\dagger \right\} = \delta_{pq}, \quad \left\{ a_p, a_q \right\} = \left\{ a_p^\dagger, a_q^\dagger \right\} = 0, \tag{10}$$

where $\{x, y\} = xy + yx$ and the indices refer to the single-particle states of the Hartree-Fock basis. For organizing the excited states of our nucleus, it is convenient to *normal order* relevant operators with respect to the reference state $|\Phi\rangle$. We define a normal-ordered one-body operator as

$$:a_p^\dagger a_q: \equiv a_p^\dagger a_q - \overbracket{a_p^\dagger a_q}, \tag{11}$$

where $\overbracket{a_p^\dagger a_q}$ is a so-called (Wick) contraction between a creation and an annihilation operator. For Slater determinant references, we have

$$\overbracket{a_p^\dagger a_q} \equiv \rho_{qp} \equiv \langle \Phi | \, a_p^\dagger a_q \, | \Phi \rangle, \tag{12}$$

i.e., the contraction is simply given by the one-body density matrix of the nucleus. We can recursively extend the normal

ordering to higher-body operators:

$$\begin{aligned} a_p^\dagger a_q^\dagger a_s a_r &= :a_p^\dagger a_q^\dagger a_s a_r: \\ &\quad + \overbrace{a_q^\dagger a_s}\, :a_p^\dagger a_r: - \overbrace{a_p^\dagger a_s}\, :a_q^\dagger a_r: \\ &\quad + \overbrace{a_p^\dagger a_r}\, :a_q^\dagger a_s: - \overbrace{a_q^\dagger a_r}\, :a_p^\dagger a_s: \\ &\quad + \left(\overbrace{a_p^\dagger a_r}\, \overbrace{a_q^\dagger a_s} - \overbrace{a_p^\dagger a_s}\, \overbrace{a_q^\dagger a_r} \right) , \end{aligned} \tag{13}$$

$$\begin{aligned} a_p^\dagger a_q^\dagger a_r^\dagger a_u a_t a_s &= :a_p^\dagger a_q^\dagger a_r^\dagger a_u a_t a_s: \\ &\quad + \overbrace{a_r^\dagger a_u}\, :a_p^\dagger a_q^\dagger a_t a_s: + \dots \\ &\quad + \left(\overbrace{a_r^\dagger a_u}\, \overbrace{a_q^\dagger a_t} - \overbrace{a_q^\dagger a_u}\, \overbrace{a_r^\dagger a_t} \right) :a_p^\dagger a_s: + \dots \\ &\quad + \overbrace{a_p^\dagger a_s}\, \overbrace{a_q^\dagger a_t}\, \overbrace{a_r^\dagger a_u} + \dots \end{aligned} \tag{14}$$

The definition (11) immediately implies that the expectation value of a normal-ordered one-body operator in the reference state vanishes, and it is straightforward to confirm that this holds for any normal-ordered operator:

$$\langle \Phi | :a_p^\dagger \dots a_q: | \Phi \rangle = 0. \tag{15}$$

This leads to significant simplifications when we evaluate expressions in MBPT or other many-body methods. In addition, any product of two normal-ordered operators can be expanded by contracting the creators and annihilators of one string with a suitable match of the other string, e.g.,

$$:a_p^\dagger a_q::a_r^\dagger a_s: = \overbrace{a_q a_r^\dagger}\, :a_p^\dagger a_s: - \overbrace{a_p^\dagger a_s}\, :a_r^\dagger a_q: + \overbrace{a_p^\dagger a_s}\, \overbrace{a_q a_r^\dagger}\, , \tag{16}$$

where we have used that[3] $:a_q a_r^\dagger: = -:a_r^\dagger a_q:$, and introduced

$$\overbrace{a_q a_r^\dagger} = \delta_{qr} - \rho_{qr}. \tag{17}$$

These are the essential rules for evaluating the MBPT expressions we are considering in the following. Additional details can be found in Refs. [6,7,9,49], for example.

3.2 The normal-ordered Hamiltonian

Since nuclei are self-bound objects, the nuclear many-body Hamiltonian is constructed using the *intrinsic kinetic energy*[4]

$$T_{\rm int} \equiv T - T_{\rm cm} \equiv T_1 + T_2. \tag{18}$$

[3] The contraction explicitly accounts for the contribution of the nonvanishing RHS of the fundamental anticommutator Eq. (10) so that we only need to track signs when we permute operators within a normal-ordered string.

[4] In particle-number conserving approaches, it can equivalently be written as a sum of two-body operators alone, but this has a subtle impact on HF and MBPT—see Refs. [50,51].

Considering two- and three-nucleon interactions, which is standard nowadays, we have a starting Hamiltonian of the form

$$H = T_1 + T_2 + V_2 + V_3. \tag{19}$$

It can be written in normal-ordered form as

$$\begin{aligned} H &= E_{\rm ref} + \sum_{pq} H_{pq} :a_p^\dagger a_q: + \frac{1}{4} \sum_{pqrs} H_{pqrs} :a_p^\dagger a_q^\dagger a_s a_r: \\ &\quad + \frac{1}{36} \sum_{pqrstu} H_{pqrstu} :a_p^\dagger a_q^\dagger a_r^\dagger a_u a_t a_s: , \end{aligned} \tag{20}$$

with

$$E_{\rm ref} = \langle \Phi | H | \Phi \rangle , \tag{21}$$

$$\begin{aligned} H_{pq} &= T_{pq} + \sum_{rs} (T+V)_{prqs} \rho_{sr} \\ &\quad + \frac{1}{2} \sum_{rstu} V_{prsqtu} \rho_{tr} \rho_{us} , \end{aligned} \tag{22}$$

$$H_{pqrs} = (T+V)_{pqrs} + \sum_{tu} V_{pqtrsu} \rho_{ut} , \tag{23}$$

$$H_{pqrstu} = V_{pqrstu} . \tag{24}$$

Here, we assume that all two- and three-body matrix elements are fully antisymmetrized under permutations of the indices, e.g.,

$$O_{pqrs} = -O_{qprs} = -O_{pqsr} = O_{qpsr} , \tag{25}$$

where $O = H, T, V$. Analogous relations hold for general observables.

Due to the normal ordering, the dominant effects of the three-nucleon interaction are absorbed into the zero-, one-, and two-body parts of the normal-ordered Hamiltonian, and we can neglect the residual three-body terms in the following. This so-called normal-ordered two-body approximation (NO2B) is frequently used in state-of-the-art nuclear many-body calculations. It significantly reduces the storage and computational effort at the cost of a typical approximation error of 1–2% in medium-mass nuclei [52,53].

The normal-ordered Hamiltonian can be simplified if we use the HF orbitals of our reference state $|\Phi\rangle$ as our single-particle basis: Then the one-body part of the Hamiltonian and the one-body density matrix are both diagonal,

$$H_{pq} = \epsilon_p \delta_{pq} , \tag{26}$$

$$\rho_{pq} = n_p \delta_{pq} , \tag{27}$$

and their eigenvalues define the single-particle energies ϵ_p and the occupation numbers n_p, respectively. In a HF state for a given nucleus with Z protons and N neutrons, the Z

proton and N neutron states with the lowest single-particle energies are occupied ($n_p = 1$) while all other single-particle states are unoccupied ($n_p = 0$). In a typical calculation, the number of occupied states is much smaller than the number of unoccupied states, $N_o \ll N_u \sim N$, where $N = N_u + N_o$ is the single-particle basis size.

Adopting a convention from quantum chemistry, we will use indices $i, j, k, \ldots$ to label occupied ("hole") states in subsequent expressions, while unoccupied ("particle") states are indicated by $a, b, \ldots$, and $p, q, \ldots$ do not distinguish between the two types of states and encompass the entire single-particle basis.

3.3 Energy corrections

Using the reference state as a basis, we can construct perturbative corrections to the wave function and energies in the usual Møller-Plesset scheme (see, e.g., [9,54]). We partition the Hamiltonian into

$$H = H_{\text{ref}} + g H_{\text{pert}}, \tag{28}$$

where

$$H_{\text{ref}} = E_{\text{ref}} + \sum_p \epsilon_p :a_p^\dagger a_p: , \tag{29}$$

$$H_{\text{pert}} = \frac{1}{4} \sum_{pqrs} H_{pqrs} :a_p^\dagger a_q^\dagger a_s a_r: \tag{30}$$

and g is merely a book-keeping parameter that will be set to 1 in practical calculations. Formally, the energy and the many-body state are then expanded as

$$E = E^{(0)} + g E^{(1)} + g^2 E^{(2)} + \ldots \tag{31}$$

$$|\Psi\rangle = |\Psi^{(0)}\rangle + g\,|\Psi^{(1)}\rangle + g^2\,|\Psi^{(2)}\rangle + \ldots \tag{32}$$

where the corrections $|\Psi^{(k)}\rangle$ for $k > 0$ are supposed to be orthogonal to the leading-order wave function:

$$\langle \Psi^{(0)} | \Psi^{(k)} \rangle = 0. \tag{33}$$

Plugging the expansions into the Schrödinger equation,

$$\begin{aligned} &(H_{\text{ref}} + g H_{\text{pert}}) \left(|\Psi^{(0)}\rangle + g\,|\Psi^{(1)}\rangle + \ldots \right) \\ &= (E^{(0)} + g E^{(1)} + \ldots) \left(|\Psi^{(0)}\rangle + g\,|\Psi^{(1)}\rangle + \ldots \right) , \end{aligned} \tag{34}$$

and comparing powers of g, one immediately obtains

$$H_{\text{ref}}\,|\Psi^{(0)}\rangle = E^{(0)}\,|\Psi^{(0)}\rangle = E_{\text{ref}}\,|\Psi^{(0)}\rangle. \tag{35}$$

The energy corrections can now be obtained by projecting onto the unperturbed state,

$$E^{(k)} = \langle \Psi^{(0)}|\, H_{\text{pert}}\,|\Psi^{(k-1)}\rangle, \tag{36}$$

and the wave function corrections are given by

$$\begin{aligned} |\Psi^{(k)}\rangle = &\frac{Q}{E_{\text{ref}} - H_{\text{ref}}} H_{\text{pert}}\,|\Psi^{(k-1)}\rangle \\ &- \sum_{j=1}^{k-1} E^{(j)} \frac{Q}{E_{\text{ref}} - H_{\text{ref}}}\,|\Psi^{(k-j)}\rangle , \end{aligned} \tag{37}$$

where the projection operator

$$Q = 1 - |\Psi^{(0)}\rangle\langle\Psi^{(0)}| \tag{38}$$

was introduced to ensure that Eq. (33) holds at all orders.

In the canonical MBPT with a Hartree-Fock Slater determinant reference state $|\Phi\rangle$, we have

$$E^{(0)} = E_{\text{ref}}, \quad |\Psi^{(0)}\rangle = |\Phi\rangle. \tag{39}$$

Because H_{pert} is in normal order, $E^{(1)} = \langle\Phi|\, H_{\text{pert}}\,|\Phi\rangle = 0$ and the first correction to the energy appears at second order. The corrections are expanded in terms of particle-hole excitations of the reference state:

$$|\Phi_{ij\ldots}^{ab\ldots}\rangle = a_a^\dagger a_b^\dagger \ldots a_j a_i\,|\Phi\rangle = :a_a^\dagger a_b^\dagger \ldots a_j a_i: |\Phi\rangle, \tag{40}$$

where we have used that contractions between particle ($a, b, \ldots$) and hole indices ($i, j, \ldots$) vanish. The vanishing expectation value of normal-ordered operators in the reference state (see Eq. (15)) guarantees that the orthogonality condition (33) is satisfied. Furthermore, the particle-hole excitations are eigenstates of H_{ref} with

$$\begin{aligned} H_{\text{ref}}\,|\Phi_{ij\ldots}^{ab\ldots}\rangle &= (E_{\text{ref}} + \epsilon_a + \epsilon_b + \ldots - \epsilon_i - \epsilon_j)\,|\Phi_{ij\ldots}^{ab\ldots}\rangle \\ &\equiv (E_{\text{ref}} + \epsilon_{ij\ldots}^{ab\ldots})\,|\Phi_{ij\ldots}^{ab\ldots}\rangle , \end{aligned} \tag{41}$$

where we have introduced the compact notation $\epsilon_{ij\ldots}^{ab\ldots}$ for single-particle energy differences.

Starting from a Hartree-Fock Slater determinant $|\Phi\rangle$, we can write the many-body wave function through first order as

$$\begin{aligned} |\Psi\rangle = &|\Phi\rangle - \frac{1}{4} g \sum_{abij} \frac{H_{abij}}{\epsilon_{ij}^{ab}} :a_a^\dagger a_b^\dagger a_j a_i: |\Phi\rangle \\ &+ O(g^2) . \end{aligned} \tag{42}$$

Since H is Hermitian, $H_{ijab} = \overline{H_{abij}}$ and the energy through second order can be written as

$$E = E_{\text{ref}} - \frac{1}{4} g^2 \sum_{abij} \frac{|H_{abij}|^2}{\epsilon_{ij}^{ab}} + O(g^3). \tag{43}$$

3.4 General observables

For observables other than the energy, we consider the perturbative expansion of the expectation value

$$\langle O\rangle = \frac{\langle\Psi|\, O\,|\Psi\rangle}{\langle\Psi|\Psi\rangle}. \tag{44}$$

Treating the denominator first, we obtain

$$\frac{1}{\langle\Psi|\Psi\rangle} = 1 - g^2\langle\Psi^{(1)}|\Psi^{(1)}\rangle + O(g^4), \tag{45}$$

hence

$$\begin{aligned}\langle O\rangle &= \langle\Psi^{(0)}|\, O\,|\Psi^{(0)}\rangle \\ &\quad + g\left(\langle\Psi^{(1)}|\, O\,|\Psi^{(0)}\rangle + \langle\Psi^{(0)}|\, O\,|\Psi^{(1)}\rangle\right) \\ &\quad + g^2\Big(\langle\Psi^{(1)}|\, O\,|\Psi^{(1)}\rangle - \langle\Psi^{(0)}|\, O\,|\Psi^{(0)}\rangle\langle\Psi^{(1)}|\Psi^{(1)}\rangle \\ &\quad + \langle\Psi^{(2)}|\, O\,|\Psi^{(0)}\rangle + \langle\Psi^{(0)}|\, O\,|\Psi^{(2)}\rangle\Big) \\ &\quad + O(g^3)\,.\end{aligned} \tag{46}$$

Let us now plug in the operator O in normal ordered form:

$$O = O_0 + O_1 + O_2, \tag{47}$$

where the subscript again indicates the particle rank of the operator. Then we have

$$O_0 = \langle\Psi^{(0)}|\, O\,|\Psi^{(0)}\rangle \tag{48}$$

because of Eq. (15) and $\langle\Psi^{(0)}|\Psi^{(0)}\rangle = 1$. Since the perturbation is a two-body operator, we also note that

$$\langle\Psi^{(1)}|\, O\,|\Psi^{(0)}\rangle = \langle\Psi^{(1)}|\, O_2\,|\Psi^{(0)}\rangle = \overline{\langle\Psi^{(0)}|\, O\,|\Psi^{(1)}\rangle}\,, \tag{49}$$

$$\langle\Psi^{(2)}|\, O\,|\Psi^{(0)}\rangle = \langle\Psi^{(2)}|\, O_2\,|\Psi^{(0)}\rangle = \overline{\langle\Psi^{(0)}|\, O\,|\Psi^{(2)}\rangle}\,, \tag{50}$$

$$\begin{aligned}\langle\Psi^{(1)}|\, O\,|\Psi^{(1)}\rangle &= O_0\langle\Psi^{(1)}|\Psi^{(1)}\rangle + \langle\Psi^{(1)}|\, O_1\,|\Psi^{(1)}\rangle \\ &\quad + \langle\Psi^{(1)}|\, O_2\,|\Psi^{(1)}\rangle\,.\end{aligned} \tag{51}$$

Thus, in Eq. (46) the $O(g^2)$ terms proportional to O_0 cancel, the one-body operator O_1 appears at second order, and O_2 at first order.

Evaluating the individual terms according to the rules discussed above, we find that perturbative corrections through $O(g^2)$ are

$$\begin{aligned}O_1^{(2)} &= \langle\Psi^{(1)}|\, O_1\,|\Psi^{(1)}\rangle \\ &= \frac{1}{2}\sum_{abcij}\frac{H_{ijab}O_{ac}H_{cbij}}{\epsilon_{ij}^{ab}\epsilon_{ij}^{cb}} - \frac{1}{2}\sum_{abijk}\frac{H_{abij}O_{ik}H_{kjab}}{\epsilon_{ij}^{ab}\epsilon_{kj}^{ab}}\,,\end{aligned} \tag{52}$$

$$\begin{aligned}O_2^{(1)} &= \langle\Psi^{(1)}|\, O_2\,|\Psi^{(0)}\rangle + \langle\Psi^{(0)}|\, O_2\,|\Psi^{(1)}\rangle \\ &= -\frac{1}{4}\sum_{abij}\frac{O_{ijab}H_{abij} + H_{ijab}O_{abij}}{\epsilon_{ij}^{ab}}\,,\end{aligned} \tag{53}$$

and

$$\begin{aligned}O_2^{(2)} &= \langle\Psi^{(1)}|\, O_2\,|\Psi^{(1)}\rangle + \langle\Psi^{(0)}|\, O_2\,|\Psi^{(2)}\rangle \\ &\quad + \langle\Psi^{(2)}|\, O_2\,|\Psi^{(0)}\rangle \\ &= \frac{1}{8}\sum_{abcdij}\frac{H_{ijab}O_{abcd}H_{cdij}}{\epsilon_{ij}^{ab}\epsilon_{ij}^{cd}} \\ &\quad + \frac{1}{8}\sum_{abijkl}\frac{H_{abkl}O_{klij}H_{ijab}}{\epsilon_{ij}^{ab}\epsilon_{kl}^{ab}} \\ &\quad - \sum_{abcijk}\frac{H_{ijab}O_{kbic}H_{ackj}}{\epsilon_{ij}^{ab}\epsilon_{kj}^{ac}} + (O\leftrightarrow H)\,,\end{aligned} \tag{54}$$

where the short-hand in the last line indicates permutations of the first three terms in which O is swapped with one of the Hamiltonian operators H.

We can readily verify that the application of this approach to the Hamiltonian will yield the second-order energy from the previous section: Since $O_1 = H_{\text{ref}} - E_{\text{ref}}$, we find after some index manipulation that

$$H_1^{(2)} = \frac{1}{2}\sum_{abij}\frac{|H_{abij}|^2}{(\epsilon_{ij}^{ab})^2}(\epsilon_a - \epsilon_i) = \frac{1}{4}\sum_{abij}\frac{|H_{abij}|^2}{(\epsilon_{ij}^{ab})^2}\epsilon_{ij}^{ab}, \tag{55}$$

and with $O_2 = gH_{\text{pert}}$ the leading two-body term becomes

$$H_2^{(2)} = -\frac{1}{2}\sum_{abij}\frac{|H_{abij}|^2}{\epsilon_{ij}^{ab}}. \tag{56}$$

Plugging everything into Eq. (46), we obtain the second-order energy (43).

We conclude this section by emphasizing an important difference between the perturbative treatment of the Hamiltonian and that of a general observable. The normal-ordered zero- and one-body parts of H are treated exactly because the working basis for the expansion are the eigenfunctions of H_{ref} (cf. Eq. (41)), and only the two-body part of H is treated perturbatively. This is not the case for a general observable O. In essence, we have to view (44) as a sum of separate expansions for the different normal-ordered contributions of O, each of which might have their own order-by-order convergence behavior. As we will see in a concrete application below, the second-order contribution to $\langle O_1\rangle$ can be greater than the first-order contribution to $\langle O_2\rangle$, and therefore the dominant perturbative correction to the expectation value (46).

4 Modeling perturbative correction terms as inner products

This section provides a framework for modeling perturbative corrections to nuclear ground-state energies and observables as the sum of multiple inner products between tensors, so that each inner product can be approximated according to the geometry-preserving property of JLEs as outlined in Lemma 1. The idea is to calculate the inner product of tensors with reduced dimensions to obtain an approximate value of the exact results. In doing so, it is assumed that the data lie on a low-rank Hilbert space of tensors.

4.1 Second-order energy correction

For the sake of brevity, we define and use the following real-valued tensor from the energy denominators in the perturbative expressions:

$$D_{pqrs} \equiv \begin{cases} \frac{1}{\epsilon_p+\epsilon_q-\epsilon_r-\epsilon_s} & \text{if } n_p = n_q = 0 \text{ and} \\ & n_r = n_s = 1\,, \\ 0 & \text{else}\,. \end{cases} \tag{57}$$

Thus, the entries of the tensor D vanish unless the first two indices refer to particle states, and the last two to hole states. It will allow us to extend sums that are restricted to either class of states to the entire single-particle basis in the following, e.g.,

$$\sum_{abij} \frac{H_{ijab} H_{abij}}{\epsilon^{ab}_{ij}} = \sum_{pqrs} H_{rspq} D_{pqrs} H_{pqrs}. \tag{58}$$

In the following, we assume spherical symmetry for the nucleus and adopt an angular-momentum coupled representation, the so-called J-scheme. While we will use the same notation as in the discussion above to avoid clutter, the indices p no longer represent individual single-particle states, but groups of energetically degenerate single-particle levels that are characterized by a tuple of radial, orbital angular momentum, angular momentum, and isospin quantum numbers[5]:

$$p = (\nu_p, l_p, j_p, \tau_p). \tag{59}$$

As a consequence, the two-body tensors will have a block structure that we indicate by using the total angular momentum quantum number J, e.g., H^J_{pqrs}. Physically allowed entries of the tensors must satisfy the conditions

$$|j_p - j_q| \le J \le j_p + j_q\,, \quad |j_r - j_s| \le J \le j_r + j_s\,. \tag{60}$$

[5] We denote the radial quantum number with a ν instead of the usual n to avoid confusion with the occupation numbers. Individual single-particle states carry the projection m_p of j_p as quantum numbers in addition to the tuple p.

In the uncoupled representation, we would have $2J+1$ copies of each reduced tensor H^J_{pqrs}, and accordingly, these multiplicities will appear as explicit factors in subsequent expressions.

In the J-scheme, the second-order energy correction term is defined as:

$$E^{(2)} = \sum_{J=0}^{J_{\max}} E^{(2)}(J)\,, \tag{61}$$

where $J_{\max}$ is the largest total angular momentum that can be obtained by coupling the single-particle angular momenta, and

$$\begin{aligned} E^{(2)}(J) &= -\frac{1}{4}(2J+1) \sum_{abij} H^J_{abij} D^J_{abij} H^J_{ijab} \\ &= -\frac{1}{4}(2J+1)\, \langle \widetilde{H}^J, H^J \rangle. \end{aligned} \tag{62}$$

Here, we have written the energy correction in terms of the inner product (2) to set the stage for applying the JL lemma, and we have introduced $\widetilde{H}^J$ as an element-wise product of D^J with H^J, i.e.,

$$\widetilde{H}^J_{pqrs} = D^J_{pqrs} H^J_{pqrs}. \tag{63}$$

An approximation of Eq. (62) can be computed by randomly projecting H^J and $\widetilde{H}^J$ onto a lower-dimensional space using mode-wise JL embeddings:

$$\widehat{H}^J = H^J \bigtimes_{\ell=1}^{4} \mathbf{A}^{(\ell)}, \tag{64}$$

and

$$\widehat{\widetilde{H}}^J = \widetilde{H}^J \bigtimes_{\ell=1}^{4} \mathbf{A}^{(\ell)}, \tag{65}$$

where $\mathbf{A}^{(k)} \in \mathbb{R}^{m_k \times N}$ are JL matrices and $m_k \le N$ for $k \in [4]$. Now, with high probability,

$$\langle \widetilde{H}^J, H^J \rangle \approx \langle \widehat{\widetilde{H}}^J, \widehat{H}^J \rangle, \tag{66}$$

to within an adjustable error that is related to the target dimension sizes m_j.

A second-stage JL embedding can be applied to the vectorized versions of H^J and $\widetilde{H}^J$ to further compress the projected tensors before computing the approximate inner product. This is achieved by calculating

$$\widehat{\mathbf{h}} = \mathbf{A}\, \mathrm{vect}\left(\widehat{H}^J\right), \tag{67}$$

where $\widehat{\mathbf{h}} \in \mathbb{R}^m$ and $\mathbf{A} \in \mathbb{R}^{m \times \prod_{k=1}^4 m_k}$. The same operation is performed on $\widehat{\widetilde{H}}^J$ to obtain $\widehat{\widetilde{\mathbf{h}}}$.

4.2 Radius corrections

To explore the impact of the JL embeddings on observables, we consider the mean-square radius operator[6]

$$R \equiv \frac{1}{A}\sum_{i=1}^{A}(\mathbf{r}_i - \mathbf{r}_{\mathrm{cm}})^2\,, \tag{68}$$

with

$$\mathbf{r}_{\mathrm{cm}} = \frac{1}{A}\sum_{i=1}^{A}\mathbf{r}_i\,. \tag{69}$$

We write it as a sum of one- and two-body operators,

$$R = \frac{1}{A}\left(\left(1-\frac{1}{A}\right)\sum_i \mathbf{r}_i^2 - \frac{1}{A}\sum_{i\neq j}\mathbf{r}_i\cdot\mathbf{r}_j\right)\,, \tag{70}$$

and normal order it with respect to the Hartree-Fock reference state $|\Phi\rangle$ before plugging it into Eqs. (52) and (53) to evaluate the leading radius corrections. In the following, we discuss how the individual contributions can be written as inner products along the lines of Eq. (62).

4.2.1 One-body operator, particle term

The first one-body correction term in Eq. (52) contains a sum over the particle matrix elements R_{ac} of the normal-ordered one-body part of the radius operator. It can be expressed in the following way:

$$\begin{aligned}
R_I &= \frac{1}{2}\sum_J (2J+1)\sum_{abcij} H^J_{ijab} D_{abij} R_{ac} D_{cbij} H^J_{cbij} \\
&= \frac{1}{2}\sum_J (2J+1)\sum_{abcij} \overline{H^J_{abij}} D_{abij} R_{ac} D_{cbij} H^J_{cbij} \\
&= \frac{1}{2}\sum_J (2J+1)\sum_{abcij} \overline{\widetilde{H}^J_{abij}} R_{ac} \widetilde{H}^J_{cbij} \\
&= \frac{1}{2}\sum_J (2J+1)\sum_{abij} \overline{\widetilde{H}^J_{abij}} X^J_{abij} \\
&= \frac{1}{2}\sum_J (2J+1)\left\langle X^J, \widetilde{H}^J\right\rangle,
\end{aligned} \tag{71}$$

where $\widetilde{H}$ is defined as in Eq. (63), and we have used that D is real-valued, and H is Hermitian. Note that the relation

$$X^J_{pqrs} = \sum_a R_{pa}\widetilde{H}^J_{aqrs} = \sum_t R_{pt}\widetilde{H}^J_{tqrs}. \tag{72}$$

holds for the newly introduced tensor X due to the properties of D (cf. Eq. (57)). We also observe that

$$X^J = \widetilde{H}^J \times_1 \mathbf{R}, \tag{73}$$

where $\mathbf{R}$ is the matrix of coefficients of the one-body part of the normal-ordered radius operator. Combining everything, the approximate particle term can be calculated as

$$R_I \approx \frac{1}{2}\sum_J (2J+1)\langle \widehat{X}^J, \widehat{\widetilde{H}}^J\rangle, \tag{74}$$

where

$$\widehat{\widetilde{H}}^J = \widetilde{H}^J \bigtimes_{\ell=1}^{4} \mathbf{A}^{(\ell)}, \tag{75}$$

and

$$\widehat{X}^J = X^J \bigtimes_{\ell=1}^{4} \mathbf{A}^{(\ell)} = \widetilde{H}^J \times_1 \left(\mathbf{A}^{(1)}\mathbf{R}\right) \bigtimes_{\ell=2}^{4} \mathbf{A}^{(\ell)}. \tag{76}$$

4.2.2 One-body operator, hole term

The calculation of the second term is very similar to that for the first term—we do need to be mindful that the summation now involves the hole matrix elements R_{ik}:

$$\begin{aligned}
R_{II} &= \frac{1}{2}\sum_J (2J+1)\sum_{abijk} H^J_{abij} D_{abij} H^J_{kjab} D_{abkj} R_{ik} \\
&= \frac{1}{2}\sum_J (2J+1)\sum_{abijk} \widetilde{H}^J_{abij} R_{ik} \overline{\widetilde{H}^J_{abkj}} \\
&= \frac{1}{2}\sum_J (2J+1)\sum_{abij} Y^J_{abij} \overline{\widetilde{H}^J_{abij}} \\
&= \frac{1}{2}\sum_J (2J+1)\left\langle Y^J, \widetilde{H}^J\right\rangle,
\end{aligned} \tag{77}$$

where we have introduced

$$Y^J_{pqrs} = \sum_i \widetilde{H}^J_{pqis} R_{ir} = \sum_t \widetilde{H}^J_{pqts} R_{tr}. \tag{78}$$

We can again rely on the properties of $\widetilde{H}^J$ and D to write the sum over holes as an unrestricted sum over the single-particle indices. Since

$$Y^J = \widetilde{H}^J \times_3 \mathbf{R}^\top, \tag{79}$$

we can define

$$\begin{aligned}
\widehat{Y}^J &= Y^J \bigtimes_{\ell=1}^{4} \mathbf{A}^{(\ell)} \\
&= \widetilde{H}^J \times_1 \mathbf{A}^{(1)} \times_2 \mathbf{A}^{(2)} \times_3 (\mathbf{A}^{(3)}\mathbf{R}^\top) \times_4 \mathbf{A}^{(4)}
\end{aligned} \tag{80}$$

[6] We suppress the exponent of the operator to reduce clutter in subsequent expressions.

Table 1 Basis truncation parameters and mode dimensions for single-particle bases labeled by $e_{\max}$ in the following. For $e_{\max} = 12, 14$ we introduce an additional truncation on the single-particle orbital angular momentum, $l \leq l_{\max} = 10$. See text for details

$e_{\max}$	4	6	8	10	12*	14*
Dimension	30	56	90	132	174	216

and write the approximate hole term as

$$R_{II} \approx \frac{1}{2} \sum_J (2J+1) \langle \widehat{Y}^J, \widehat{\widetilde{H}}^J \rangle. \tag{81}$$

4.2.3 Two-body operator

The leading radius correction from the normal-ordered two-body operator, Eq. (53), has the same structure as the second-order energy correction. Using the Hermiticity of H and R, we have

$$\begin{aligned} R_2^{(1)} &= -\frac{1}{2} \sum_J (2J+1) \sum_{abij} \Re \left(R^J_{abij} \widetilde{H}^J_{abij} \right) \\ &= -\frac{1}{2} \sum_J (2J+1) \Re \left(\langle R^J, \widetilde{H}^J \rangle \right), \end{aligned} \tag{82}$$

and after projection,

$$R_2^{(1)} \approx -\frac{1}{2} \sum_J (2J+1) \Re \left(\langle \widehat{R}^J, \widehat{\widetilde{H}}^J \rangle \right). \tag{83}$$

5 Applications

In this section, numerical results are provided to demonstrate how modewise JLEs affect the accuracy of MBPT calculations.

5.1 Preliminaries

5.1.1 Interactions and single-particle bases

We perform Hartree-Fock and MBPT(2) calculations in spherical harmonic oscillator working bases that are characterized by the oscillator frequency $\hbar\omega$ and the energy quantum number $e = 2\nu + l$, where ν and l are the oscillator's radial and orbital angular momentum quantum numbers, respectively. The basis is truncated by imposing $e \leq e_{\max}$. For $e_{\max} > 10$, we introduce an additional truncation $l \leq l_{\max} = 10$ that further reduces the single-particle basis dimension. Table 1 summarizes these basis dimensions—and therefore the mode dimensions—for the different values of $e_{\max}$ we consider in the following (also see Sect. 4).

For a given $e_{\max}$ and $l_{\max}$, the total angular momentum J is restricted by

$$0 \leq J \leq 2 \ \min(e_{\max}, l_{\max}) + 1. \tag{84}$$

Our starting Hamiltonians consist of two- and three-nucleon interactions from Chiral Effective Field Theory. In particular, we will consider the family of interactions introduced in [55,56], which we label as EMλ/Λ for short in the following. They consist of the chiral N^{3}LO nucleon-nucleon interaction by Entem and Machleidt, whose resolution scale λ has been lowered by Similarity Renormalization Group evolution [57], and an N^{2}LO three-nucleon interaction with momentum cutoff Λ whose parameters have been adjusted to fit the binding energy and charge radius of ^{4}He.

We handle the enormous memory requirements of the three-nucleon interaction in the usual way, by introducing a truncation on the energy of harmonic oscillator three-nucleon states:

$$e_1 + e_2 + e_3 \leq \min(3e_{\max}, E_{3,\max}). \tag{85}$$

In the present work, all calculations were performed with $E_{3,\max} = 14$. For the interactions of the EMλ/Λ family, this is sufficient to achieve converged results for ground-state observables in nuclei up to mass 50–60, while it is necessary to extend $E_{3,\max}$ to values in the range of 24–28 to achieve full convergence for nuclei like ^{78}Ni or ^{132}Sn, which are among the cases we examine in the following [58,59]. However, this is not an issue because here we are interested in assessing the performance of the JLE as an ingredient in specific numerical calculations instead of the accurate description of experimental data.

The solution of the Hartree-Fock equations is used as a reference state to normal order the Hamiltonian and other observables (cf. Sect. 3.2). We switch to the HF single-particle basis and employ the commonly used normal-ordered two-body approximation (NO2B) (cf. Sect. 3.2 and Refs. [6,48,53]), discarding the residual normal ordered three-nucleon operators in the evaluation of MBPT corrections. In the medium-mass nuclei we are considering in the following, this causes a systematic error of about 1–2% in the energy and other observables [53,60]. We note that this error has no impact on the performance of the JLEs, which are the focus of the present study. In follow-up work, we will explore whether JLE-based compression can make the explicit inclusion of the truncated three-nucleon terms in MBPT and other types of many-body calculations computationally feasible.

5.1.2 Compression and error measures

For a general tensor, we can define the compression in mode k as

$$c_k = \frac{m_k}{n_k}, \tag{86}$$

where n_k and m_k denote the size of mode k before and after projection, respectively. The target dimension m_k in JL matrices is chosen as $m_k = \lceil c_k n_k \rceil$ for all k to ensure that at least a fraction c_k of the ambient dimension in mode k is preserved.

The focus of the present work is on the coefficient tensor H_{pqrs} of the normal-ordered Hamiltonian (see Sect. 3.2), since it drives the computational and storage costs of the MBPT(2) method. This tensor is not only Hermitian, but also antisymmetric under permutations $p \leftrightarrow q$ and $r \leftrightarrow s$ (cf. Eq. (25)). Thus, all of its modes have the same dimension, and we choose the same compression for all modes, i.e.,

$$n_k = N, \quad c_k = c, \quad \text{for all } k. \tag{87}$$

The total compression, denoted by c_{tot} in the following, is defined by the number of elements in a tensor after compression divided by the number of elements in the uncompressed version. For single-stage JL embeddings, it is given by

$$c_{\text{tot}} = \prod_{k=1}^{d} \frac{m_k}{n_k} = \prod_{k=1}^{d} \frac{\lceil c_k n_k \rceil}{n_k} = \frac{\lceil cN \rceil^4}{N^4}, \tag{88}$$

where $\lceil \cdot \rceil$ is the usual ceiling function, and for two-stage embeddings (cf. Sect. 4.1), we have

$$c_{\text{tot}} = \frac{\lceil c_2 \prod_{k=1}^{d} m_k \rceil}{\prod_{k=1}^{d} n_k} = \frac{\lceil c_2 \lceil cN \rceil^4 \rceil}{N^4}. \tag{89}$$

This total compression is applied uniformly in all J channels in the present study.

Next, we introduce the error measures we will be using to assess the performance of the JLEs in the following. For specific perturbative contributions, it is natural to consider the mean error

$$\overline{\Delta O} = \text{mean}\left(\left| \widehat{O} - O \right| \right), \tag{90}$$

where $\widehat{O}$ is evaluated using the projected and compressed inner products defined in Sect. 4, and we take the mean over a number of trials (typically 100 or more).

In a broader context, the measure (90) does not account for the fact that the quantities we are approximating with JLEs are mere corrections to the observables were are interested in, e.g., the total ground-state energy and mean-square radius of a nucleus. For that reason, in what follows, we will also consider

$$\overline{\Delta E} = \text{mean}\left(\left| \widehat{E} - E \right| \right), \tag{91}$$

where $E = E_0 + E^{(2)} = E_{\text{ref}} + E^{(2)}$, and

$$\overline{\Delta R} = \text{mean}\left(\left| \widehat{R} - R \right| \right), \tag{92}$$

where $R = R_0 + R_I + R_{II}$ (see Sect. 5.4).

5.2 Choice of Johnson–Lindenstrauss embedding

Many prescriptions exist for selecting the matrices $\mathbf{A}$ (cf. Definition 1) that are used as JL embeddings. For that reason, we first explore the performance of several common choices, namely Gaussian [43], Rademacher [42], and the so-called Fast JL [61] matrices. For *Gaussian JL*,

$$\mathbf{A}^{(j)} = \frac{1}{\sqrt{m_j}} \mathbf{G} \tag{93}$$

is used for all $j \in [d]$ where d is the number of modes in the tensors forming the inner product, m_j is the target dimension for mode j, and each entry in $\mathbf{G}$ is an independent and identically distributed standard Gaussian random variable $\mathbf{G}_{ij} \sim \mathcal{N}(0, 1)$. For *Rademacher JL*,

$$\mathbf{A}^{(j)} = \frac{1}{\sqrt{m_j}} \mathbf{A}, \tag{94}$$

where the elements of $\mathbf{A}$ are Rademacher random variables, i.e., they take on the values $+1$ and -1 with equal probabilities. For *Fast JL*, we will use the definitions

$$\mathbf{A}^{(j)} = \frac{1}{\sqrt{m_j}} \mathbf{RFD} \tag{95}$$

or

$$\mathbf{A}^{(j)} = \frac{1}{\sqrt{m_j}} \mathbf{RCD} \tag{96}$$

for all $j \in [d]$, where $\mathbf{R}$ denotes the random restriction matrix which uniformly picks rows from the matrix it is applied to, $\mathbf{F}$ and $\mathbf{C}$ are the unitary Discrete Fourier Transform and type-1 Discrete Cosine Transform matrices scaled by $\sqrt{n_j}$, respectively, and $\mathbf{D}$ is a diagonal matrix of Rademacher random variables [61]. The two Fast JL schemes are labeled RFD and RCD in the following. For the RFD scheme, we make the additional simplification of considering only the real part of the result when applying the Fourier matrices—we indicate this through the subscript $(\cdot)_{\text{real}}$.

In Figs. 1 and 2 we compare the performance of the aforementioned JL embeddings for the second-order energy correction in ^{16}O, using a representative chiral two- plus three-nucleon Hamiltonian. From the data shown in panels (a) and (b), it is evident that the RFD_{real} scheme emerges as the clear favorite of the four options we are considering here. If we reduce the size of the $e_{\max} = 8$ tensors' single-particle basis by 50%—roughly corresponding to $e_{\max} = 5$ (cf. Table 1)—the overall compression is $c_{\text{tot}} = 0.5^4 = 0.0625$, but

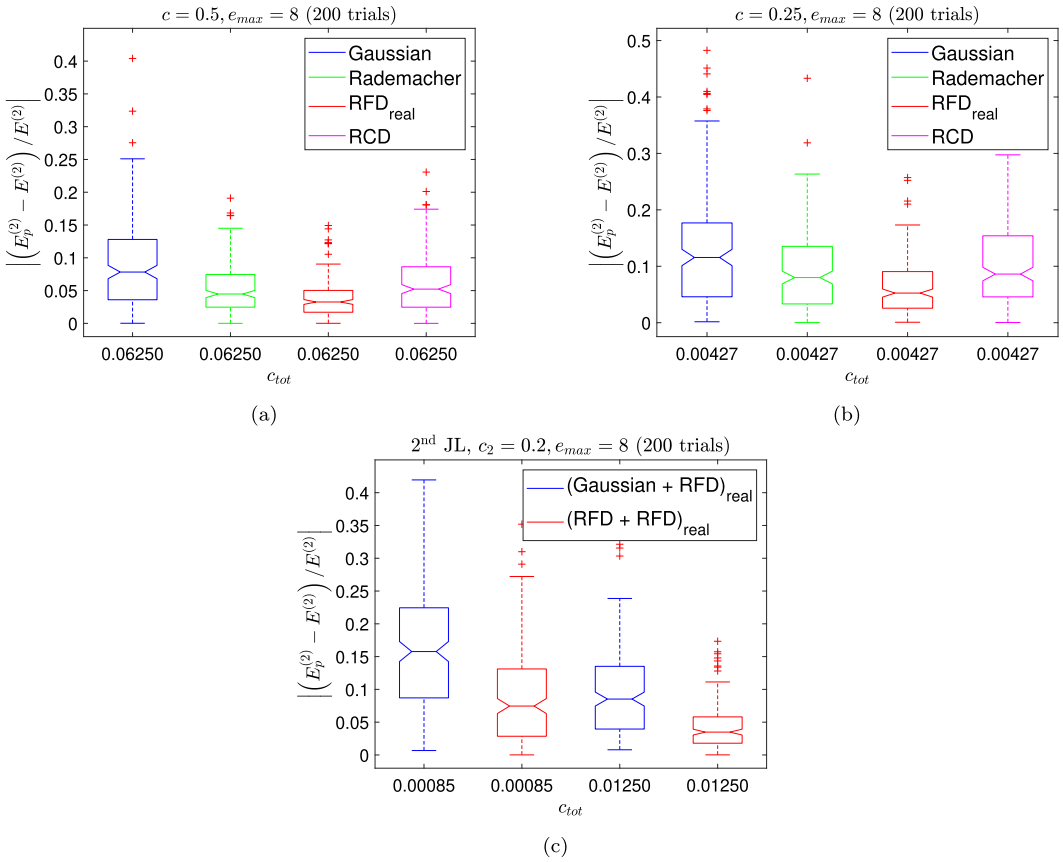

Fig. 1 Performance of different one- and two-stage JL schemes for evaluating $E^{(2)}$ in ^{16}O. In the box plots, the central mark indicates the median, and the bottom and top edges of the box indicate the 25$^{\text{th}}$ and 75$^{\text{th}}$ percentiles, respectively. The red cross symbols show the outliers.Panel **(c)** shows the impact of applying a second RFD stage of compression to the Gaussian and RFD results shown in panels **(a)** and **(b)**—see text for details. Input data were generated for the EM1.8/2.0 interaction with $e_{\max} = 8$, $\hbar\omega = 24$ MeV

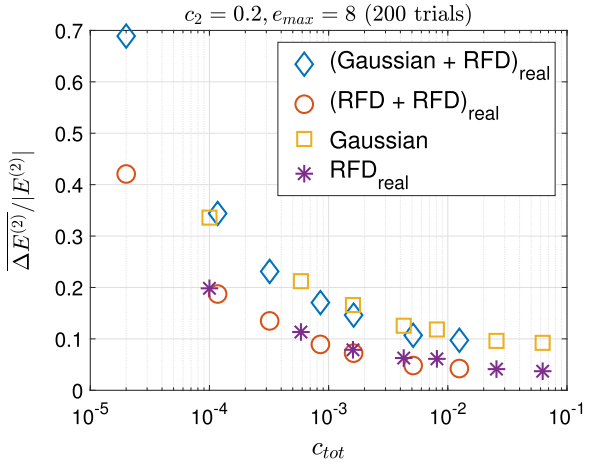

Fig. 2 Relative mean error in $E^{(2)}$ in ^{16}O as a function of the compression c_{tot} for one- and two-state JL schemes (cf. Fig. 1). Input data were generated for the EM1.8/2.0 interaction with $e_{\max} = 8$, $\hbar\omega = 24$ MeV

the median error of $E^{(2)}$ over 200 trials is only about 4%, and even the outliers do not exceed 15%. These errors correspond to ∼1–4% errors for the total MBPT(2) ground-state energy. Applying a more aggressive compression with $c = 23/90 \approx 0.255$, which makes the basis even smaller than an $e_{\max} = 4$ one, the median error for the RFD$_{\text{real}}$ scheme increases only moderately to about 5%, although the distribution of the errors spreads notably, with outliers reaching more than 20%. The increase in median error and spread of the distribution are much bigger for the other schemes.

In Fig. 1c, we show the effect of applying a second-stage JL embedding with $c_2 = 0.2$ to the Gaussian and RFD$_{\text{real}}$ JL results of panels (a) and (b). It is perhaps not surprising that an additional compression causes an increase of the median error and standard deviation of the data. Note, however, that the two-stage (RFD + RFD)$_{\text{real}}$ scheme achieves a five-fold compression over the $c_{\text{tot}} = 0.0625$ RFD$_{\text{real}}$ results to $c_{\text{tot}} = 0.0125$ while approxi-

mately maintaining the width of the error distribution and the median, which increases from 3.26% to 3.48%. For the total ground-state energy, the $(\text{RFD} + \text{RFD})_{\text{real}}$ scheme achieves sub-percent errors while only retaining 1.25% of the coefficients in the two-body part of the Hamiltonian.

In Fig. 2, we show the mean error of the one- and two-stage JL schemes used in Fig. 1c as a function of the total compression c_{tot}. Evidently, the two RFD_{real} schemes yield the lowest mean errors at a given level of compression. Since they consistently outperform the other JL methods in terms of mean, median and standard deviation of our results, we will focus on these schemes in the following, and we will use $(\text{RFD} + \text{RFD})_{\text{real}}$, in particular, because it offers the best compromise between compression and precision.

Figures 1 and 2 demonstrate the "concentration of measure" phenomenon that we touched upon in the Introduction section of this work. The large number of 100–200 trial JLE transforms for the same task lead to a small variance in the errors of the MBPT(2) energy corrections. The average absolute errors are in fact achieved by more than half the randomly generated JLE of each type, which is the case in every instance we have checked. As a result, standard averaging and medianing strategies involving only a *small* number of JLE estimates will be guaranteed to produce accurate results with overwhelming high probability. Indeed, Fig. 1c indicates that the probability that, e.g., any single $(\text{RFD} + \text{RFD})_{\text{real}}$ JLE estimator will yield more than two or three times the average reported error is only on the order of 1%—i.e., high errors are exceedingly unlikely even in the extreme case where we only evaluate a single JLE.

We want to conclude here with an observation that is relevant for future research: As discussed earlier, the mode-wise application of the matrices **FD** or **CD** (cf. Equations (95) and (96)) can be viewed as a change of the single-particle basis in which the tensors are represented, even if the restriction to real values eventually makes the transformation projective instead of unitary. Clearly, this change of basis ahead of the random sampling is beneficial, since it reduces the embedding errors. There are also a variety of physics-inspired approaches for optimizing the single-particle basis. As explained above, the Hartree-Fock basis, which is our starting representation, is obtained by minimizing the ground-state energy for a particular class of reference state, and perturbatively enhanced "natural" orbitals have recently been used for compression and convergence acceleration in nuclear many-body theory [31,32]. In future work, we will explore the interplay and possible integration of such basis optimization techniques with JLEs.

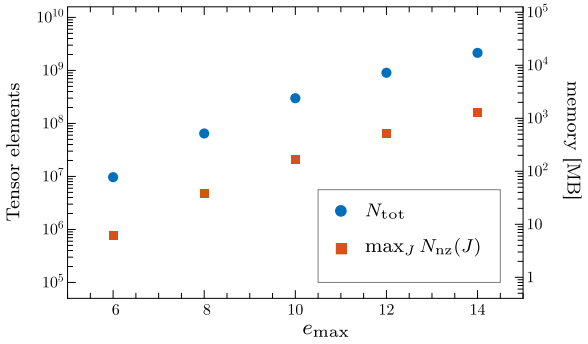

Fig. 3 Total number of Hamiltonian tensor elements, N_{tot}, and number of physically allowed nonzero entries, $\max_J N_{\text{nz}}(J)$, for each J channel as a function of the basis size $e_{\max}$. The right axis shows the associated memory required for storage. See text for details

5.3 Energy corrections

5.3.1 General features

Now that we have identified a favored JL scheme, we will proceed and explore its performance for different nuclei, basis (and tensor) sizes, and interactions. To provide context for the subsequent discussion, we first consider some general features of the Hamiltonian tensor as well as the second-order MBPT corrections.

Note that a typical single-particle basis without any symmetry restrictions can consist of well above a 1000 states, especially if it also must account for weakly bound nucleons with spatially extended single-particle wave functions. In this representation, the Hamiltonian naively would have 10^{12} or more elements, although it can be extremely sparse due to the symmetries of the interaction. For particular applications, we can impose symmetries like rotational invariance, and achieve more manageable requirements: In the J-scheme with explicit spherical symmetry (cf. Sect. 4), the tensor becomes block diagonal and the blocks with fixed angular momentum J typically range from $N_{\text{tot}} = 10^7 - 10^{10}$ elements, as illustrated in Fig. 3. Physical conservation laws for parity and isospin or charge force many of these elements to vanish and allow a reduction by an additional order of magnitude. In Fig. 3, we show the resulting number of nonzero entries N_{nz} of the largest J channel for each basis size $e_{\max}$. In a typical application, we have between 10 and 20 of these channels, and about a quarter of them have comparably large $N_{\text{nz}}(J)$, while the remaining channels are very small in comparison. As we can see, this trans-

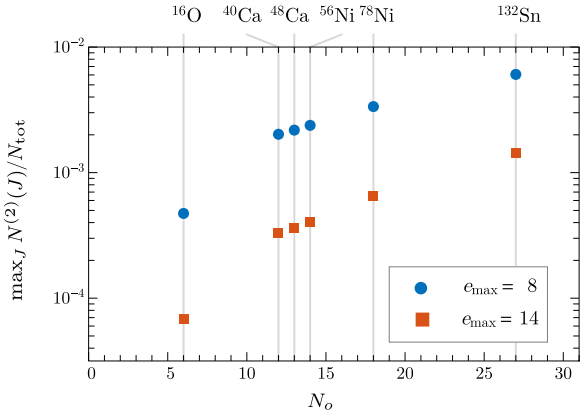

Fig. 4 Maximum fraction of Hamiltonian coefficients per J channel that can contribute to $E^{(2)}$ as a function of the number of occupied (N_o) single-particle orbitals. See text for details

lates into memory requirements in the 10 MB to 10 GB range.[7]

Switching focus to the many-body method, we recall from Sect. 3 that the first-order wave function correction $|\Psi^{(1)}\rangle$ and second-order energy correction $E^{(2)}$ only depend on a subset of elements of the Hamiltonian tensor, namely H_{abij} and H_{ijab}. As a reminder a, b refer to unoccupied (particle) orbitals, while i, j are occupied (hole) orbitals, and there are much fewer of the latter than the former, so that $N_o \ll N_u$ and $N = N_o + N_u$. The overall number of elements of the Hamiltonian that can contribute to $E^{(2)}$ (and $|\Psi^{(1)}\rangle$) will then be given by

$$N^{(2)} = 2N_o^2 N_u^2, \tag{97}$$

and the fraction of overall elements this corresponds to is

$$\frac{N^{(2)}}{N_{\rm tot}} = \frac{2N_o^2 N_u^2}{N^4}. \tag{98}$$

Since we are working in the J-scheme, N_o does not directly map to the number of nucleons because each orbital can be multiply occupied. Moreover, there is no simple analytical expression that generalizes (97) to each channel because of the angular momentum selection rule (60), although $N_{\rm tot} = N^4$ continues to hold. Counting the elements explicitly, we obtain the maximal fraction $N^{(2)}(J)/N_{\rm tot}$ across J channels for the nuclei we will discuss in the following, which is shown in Fig. 4. We see that for calcium and heavier nuclei, it lies between 0.1% and 1% for $e_{\rm max} = 8$, and it is a factor 5–6 smaller for $e_{\rm max} = 14$ because N_u grows with $e_{\rm max}$ while N_o stays constant. For the future discussion, we note that the fraction of relevant tensor elements is substantially smaller for ^{16}O than for the other nuclei, as expected because of the smaller number of occupied orbitals. Note that these numbers should be understood as upper bounds, since the natural energy scales of the interaction can limit the size of formally relevant tensor elements.

5.3.2 Second-order energy correction

In Fig. 5 we show the mean relative error of the second-order energy corrections as a function of the basis size parameter $e_{\rm max}$ for hundred- and thousandfold compressions of the Hamiltonian, considering ^{16}O and ^{132}Sn as typical examples. In our preferred two-stage JLE scheme, these compressions correspond to two- and four-fould reductions in the $e_{\rm max}$ single-particle basis size, respectively: For $c_{\rm tot} = 0.001$, this would reduce an $e_{\rm max} = 14$ basis roughly to the size of an $e_{\rm max} = 6$ basis, for example (cf. Table 1). We see that for fixed compression, the error decays exponentially with the basis size in both nuclei, and this behavior is typical for all the nuclei and interactions we studied in this work—results for additional nuclei are included in Appendix A. There are weak fluctuations because of the random character of the JL embedding, and $c_{\rm tot}$ is not strictly identical for each $e_{\rm max}$ and nucleus because of the varying dimensions (cf. Table 1).

While some of the degrees of freedom of the large $e_{\rm max}$ basis are required to achieve converged results for the HF and MBPT ground-state energies, this result shows that an ever increasing amount of elements that are irrelevant for the ground state are added to the Hamiltonian tensor as well. Consequently, we can use more aggressive compressions if we are working in larger $e_{\rm max}$ spaces.

For fixed $c_{\rm tot}$ and any given $e_{\rm max}$, the error for ^{16}O is about twice as large as for ^{132}Sn. Since the fraction of relevant tensor elements is about an order of magnitude smaller for ^{16}O than for ^{132}Sn (cf. Figure 4), the random sampling performed by the JLE might be more likely to miss relevant contributions in this nucleus. However, sparsity alone cannot be the main driver of this error, because we obtain the expected exponential decay as the sparsity increases with $e_{\rm max}$.

A breakdown of the mean relative errors by angular momentum is shown in Fig. 6. As we can see, the contributions $\overline{\Delta E^{(2)}(J)}$ all show the typical exponential decay behavior, aside from the weak fluctuations discussed above. The relative impact of the channels is roughly correlated with the distribution of $N^{(2)}(J)$: Channels around $J = 2$ or 3 typically have the highest number of relevant matrix elements and the largest contribution to the total $E^{(2)}$ in the nuclei we studied here. The $J = 0$ channel is somewhat exceptional: It has a more restricted structure because

[7] Depending on the storage format for the sparse Hamiltonian tensor, we may face significant overhead: A coordinate-based format, for instance, would have a fivefold overlap because it needs to store four indices for each element in addition to the element's value.

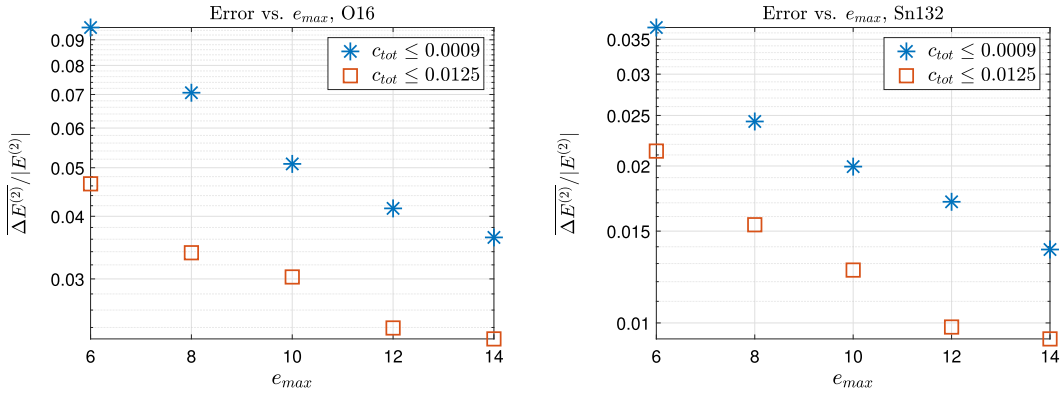

Fig. 5 Mean relative error of the second-order energy correction, $|\overline{\Delta E^{(2)}}/E^{(2)}|$, for ^{16}O and ^{132}Sn as a function of the basis size $e_{\max}$. All calculations were performed with the EM1.8/2.0 interaction, using the two-stage (RFD + RFD)$_{\text{real}}$ JL embedding and 200 trials

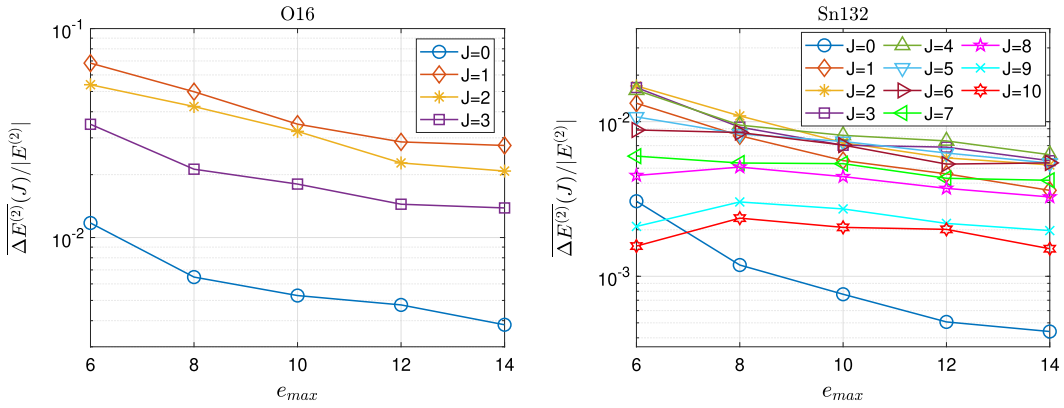

Fig. 6 Breakdown of the mean relative errors $|\overline{\Delta E^{(2)}}/E^{(2)}|$ for $c_{\text{tot}} \leq 10^{-3}$ from Fig. 6 by angular momentum channel

the angular momentum selection rules (60) force the single-particle angular momenta to be pairwise identical. Consequently, $N^{(2)}(0)$ is small, although channels with large J have even smaller $N^{(2)}(J)$. The contributions of the high-J channels to the overall error, however, are amplified because they are weighted with $2J + 1$ in Eq. (61), hence the $J = 0$ channel contribution is consistently the smallest.

For ^{16}O, only channels with $J \leq 3$ contribute to the energy correction, while channels up to $J = 10$ are relevant in ^{132}Sn because orbitals with large single-particle angular momenta are occupied. The $e_{\max} = 6$ results for ^{132}Sn exhibit deviations from the exponential behavior in the large-J channels that are artifacts of the basis truncation, but their overall impact on the error is limited. The error contributions from the individual channels are consistently larger in ^{16}O than in ^{132}Sn. Their distribution has a similar shape in both cases, although it is spread out more widely in the heavier nucleus. Thus, the greater overall error for ^{16}O cannot be caused by strong discrep-

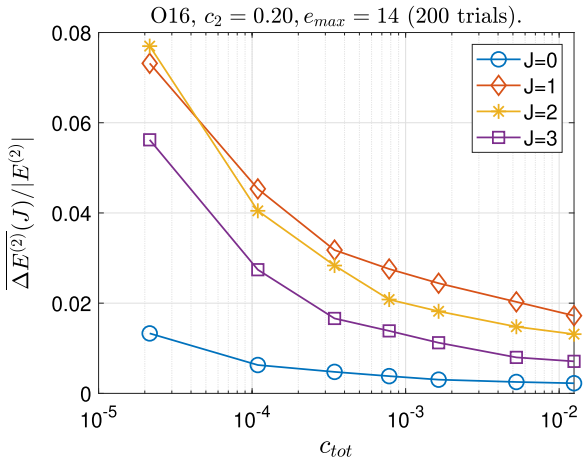

Fig. 7 Contributions of each angular momentum channel to the mean relative error $\overline{\Delta E^{(2)}}/|E^{(2)}|$ in ^{16}O as a function of the compression c_{tot} (varying c_1 but keeping a fixed compression $c_2 = 0.2$ for the second stage). Calculations were performed with the EM1.8/2.0 interaction in an $e_{\max} = 14$ basis, and a two-stage JL embedding (RFD + RFD)$_{\text{real}}$ has been used

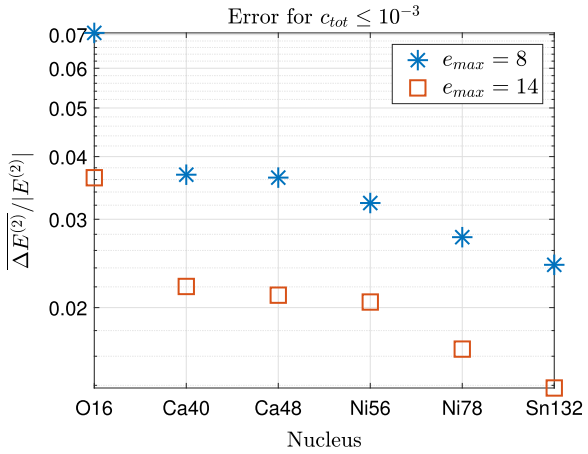

Fig. 8 Mean relative error $\overline{\Delta E^{(2)}}/|E^{(2)}|$ for several closed-shell nuclei, using $e_{\max} = 8, 14$ bases and a compression $c_{\text{tot}} \leq 10^{-3}$. All results were obtained with the EM1.8/2.0 interaction, using the (RFD + RFD)$_{\text{real}}$ embedding and carrying out 200 trials

ancies in the contributions from the low-J and high-J tails.

In Fig. 7, we explore the behavior of $\overline{\Delta E^{(2)}(J)}/|E^{(2)}|$ for ^{16}O when we keep $e_{\max} = 14$ fixed and vary c_{tot} instead. We find a smooth exponential growth of the error as we decrease c_{tot} and make the compression more aggressive. For heavier nuclei, we have more J channels to consider but the behavior is very similar—additional examples are shown in the appendix.

Figure 8 summarizes the results from applying the two-stage (RFD + RFD)$_{\text{real}}$ JL embedding with $c_{\text{tot}} \leq 10^{-3}$ to the second-order energy corrections of several closed-shell nuclei. We see that we obtain the largest and smallest mean relative errors for ^{16}O and ^{132}Sn, respectively, while the other nuclei lie inbetween. The errors for ^{40,48}Ca and ^{56}Ni are rather similar at about 2% for $e_{\max} = 14$ bases that are tyically used in production-level calculations, and the errors for ^{78}Ni and ^{132}Sn in the same basis size are in the 1–2% range.

Overall, we see that the mean relative error decreases with the particle number A. The large jump between ^{16}O and the calcium isotopes could indicate a "shell effect" as the occupation of orbitals with growing single-particle j also implies that higher J channels of the Hamiltonian can contribute. Applying the method to some sd-shell nuclei in the future could help clarify how smooth the A (or the N and Z dependencies) are, but the absence of candidate nuclei with strong shell closures means that we will have to switch to a more general form of MBPT.

5.3.3 Interaction dependence

The next aspect we want to explore is the performance of the JLE for interactions with different resolution scales. For this purpose, we have applied the (RFD + RFD)$_{\text{real}}$ embedding in calculations with other members of the EMλ/Λ family of interactions [55], specifically EM2.8/2.0 and EM2.0/2.5.

Table 2 Hartree-Fock (E_{ref}), second-order MBPT correction ($E^{(2)}$) and total MBPT(2) energy $E = E_{\text{ref}} + E^{(2)}$ of ^{16}O for three interactions from the EMλ/Λ family. All calculations were performed with $e_{\max} = 14$ at optimal $\hbar\omega$

Interaction	E_{ref} [MeV]	$E^{(2)}$ [MeV]	E [MeV]
EM1.8/2.0	− 90.29	− 33.43	− 123.72
EM2.0/2.5	− 68.78	− 44.92	− 113.70
EM2.8/2.0	− 26.20	− 83.23	− 109.43

By varying the resolution scale λ through SRG evolution (and readjusting the cutoff Λ and low-energy constants of the 3N interaction), correlations are re-shuffled between the Hartree-Fock reference state and the perturbative corrections to the wave function. As we can see for the example of ^{16}O in Table 2, the Hartree-Fock energy E_{ref} and the second-order correction $E^{(2)}$ vary by factors 3–4 for the three interactions we consider here. Note, however, that the total MBPT(2) energy only changes by about 10%. For EM1.8/2.0, the bulk of the ground-state energy is already obtained at the mean-field level, but $E^{(2)}$ is still a sizeable correction of greater than 30%, so third-order corrections are usually checked to establish convergence of the series expansion (or lack thereof). The same kind of checks are absolutely mandatory for EM2.8/2.0, since it yields an $E^{(2)}$ that is more than three times greater than E_{ref}.

In Fig. 9, we show $\overline{\Delta E^{(2)}}/|E^{(2)}|$ that result from appying the (RFD + RFD)$_{\text{real}}$ embedding to evaluate $E^{(2)}$ for our three interactions. Despite the significant differences in resolution scales and the resulting size differences in $E^{(2)}$, the mean relative errors are very similar. Since calculations with interactions like EM2.8/2.0 typically force us to use large single-particle bases to reach convergence, it is a very welcome result that we will be able to use JLEs for compression with reliable uncertainties in such applications.

5.3.4 Total energy

While the previous sections have presented a detailed analysis of JLEs in the computation of $E^{(2)}$, the quantity that is ultimately relevant for comparison with experimental data is the total energy $E = E_{\text{ref}} + E^{(2)}$ (cf. Sect. 3 and 5.1.2). In Fig. 10, we show the mean relative errors of E that result from applying the (RFD + RFD)$_{\text{real}}$ embedding with $c_{\text{tot}} \leq 10^{-3}$. Since E_{ref} is determined prior to application of the JLE, this merely amounts to a propagation of the mean absolute errors in $E^{(2)}$ to the total energy. Consequently, the behavior of the errors is very similar to what

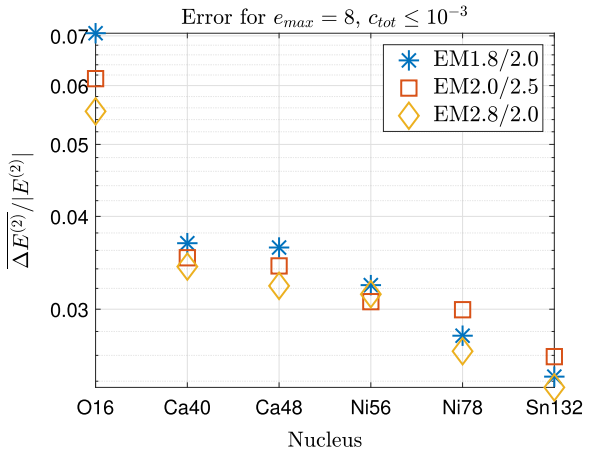

Fig. 9 Mean relative error $\overline{\Delta E^{(2)}}/|E^{(2)}|$ in various closed-shell nuclei for different members of the EMλ/Λ interaction family. All calculations were performed with an $e_{\max} = 8$ basis and compression $c_{\text{tot}} \leq 10^{-3}$, using the (RFD + RFD)$_{\text{real}}$ embedding and 200 trials

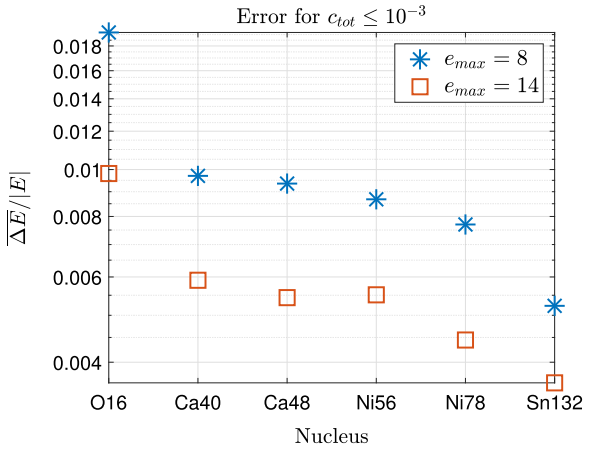

Fig. 10 Mean relative error of the total energy, $\overline{\Delta E}$, for closed-shell nuclei, using single-particle bases with $e_{\max} = 8, 14$ (at optimal $\hbar\omega$) and compression $c_{\text{tot}} \leq 10^{-3}$. All calculations were performed with the EM1.8/2.0, using (RFD + RFD)$_{\text{real}}$ and 200 trials

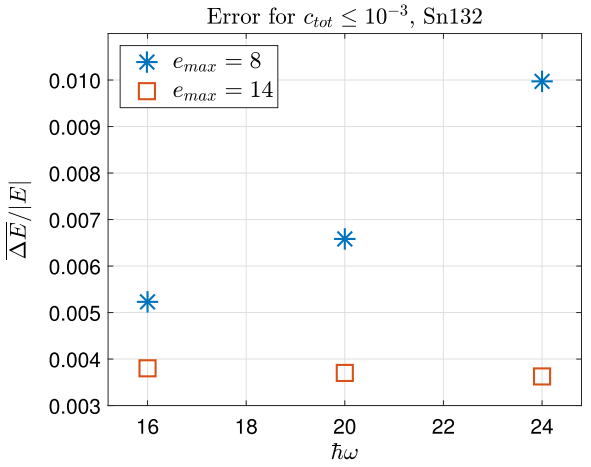

Fig. 11 Mean relative error $\overline{\Delta E}/|E|$ of ^{132}Sn as a function of $\hbar\omega$ for basis sizes $e_{\max} = 8, 14$ and compression $c_{\text{tot}} \leq 10^{-3}$. All results are obtained with EM1.8/2.0, using (RFD + RFD)$_{\text{real}}$ and 200 trials

we found in Fig. 5, but their size is reduced: The largest errors are still incurred in ^{16}O, with 2% for $e_{\max} = 8$ and 1% for $e_{\max} = 14$. For all other nuclei, even in the small basis the errors are well below 1%, and therefore much smaller than current systematic uncertainties due to the truncation of the perturbation series, NO2B approximation, or the parameters of the input interactions (see, e.g., Ref. [4]). Thus, JLEs can be used to greatly accelerate large-scale exploratory calculations that seek to quantify these uncertainties.

Since the starting point for our Hartree-Fock and subsequent MBPT(2) calculations are interaction matrix elements in a spherical harmonic oscillator basis (cf. Sect. 5.1.1), our results will in general retain some dependence on the oscillator parameter $\hbar\omega$ because of the basis' finite size. In Fig. 11, we explore this dependence for ^{132}Sn, since this nucleus requires the largest basis to achieve reasonable converge. The energy correction $E^{(2)}$ exhibits only a weak $\hbar\omega$ dependence: For instance, with $e_{\max} = 8$ and using the EM1.8/2.0 interaction, it varies from -220 MeV at $\hbar\omega = 16$ MeV to -210 MeV at $\hbar\omega = 24$ MeV. Meanwhile, the mean-field energy E_{ref} varies by 450 MeV in this window. This variation causes the typical parabolic shape that we also observe in ground-state energy convergence plots for Hartree-Fock and other many-body approaches, and it leads to significant changes in the mean relative error $\Delta E/|E|$ as well, which ranges from 0.5% to 1%. As we increase the basis size to $e_{\max} = 14$, E_{ref} is much better converged, and the error settles in at about 0.36%, consistent with Fig. 8.

Exploring the sensitivity of energies and other observables to variations of $e_{\max}$ and $\hbar\omega$ is standard practice for assessing the convergence of nuclear many-body calculations, and our present findings indicate that JLEs can be integrated into such analyses in a straighforward fashion.

5.4 Radii

While ground-state energies are typically the main quantity of interest in MBPT calculations, we can use the perturbative corrections to the wave function to evaluate other observables like the mean-square radius, as explained in Sect. 3. Formally, the leading correction to the mean-square radius is a first-order contribution from the two-body part of R (cf. Equation (70)). Upon evaluation, we find that its size is on the order of 0.01% of the reference state expec-

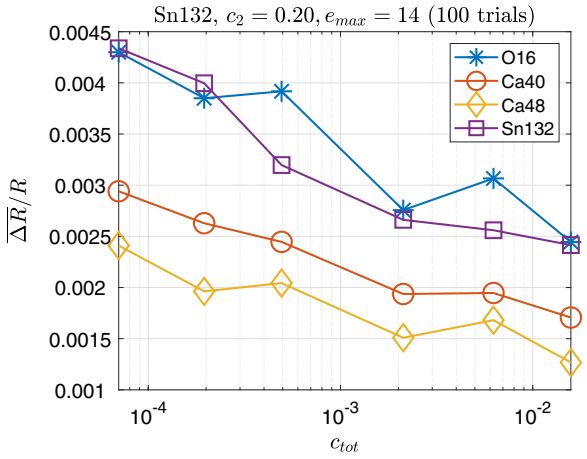

Fig. 12 Mean relative error of the total radius correction as a function of the compression (relative to the total radius correction) for various closed-shell nuclei, using the EM1.8/2.0 interaction and $e_{\max} = 14$. All results were obtained with the (RFD + RFD)$_{\text{real}}$ embedding and 100 trials, varying c_1 but keeping $c_2 = 0.2$ fixed for the second RFD stage

tation value of the operator: For instance, for ^{40}Ca with $e_{\max} = 14$, $\hbar\omega = 16$, and the EM1.8/2.0 interaction, the mean-field mean-square radius is $R_0 = 9.98\,\text{fm}^2$, and $R_2^{(1)} = 0.003\,,\text{fm}^2$. The second-order corrections from the one-body operators, on the other hand, are $R_1^{(2)} = 1.40\,\text{fm}^2$, and generally on the order of 10–15% for the nuclei studied here. For this reason, we do not consider $R_2^{(1)}$ and only focus on the one-body contributions in the following discussion.

Implementing the (RFD + RFD)$_{\text{real}}$ embedding for $R_1^{(2)}$ according to Sect. 4, we obtain the mean relative errors $\overline{\Delta R}/|R|$ shown in Fig. 12. For all the closed-shell nuclei considered here, the errors decay exponentially (up to fluctuations due to the random sampling), just like in the case of the energies. For target compressions of $c_{\text{tot}} \leq 10^{-3}$ to 10^{-2} that we discussed before, the errors are on the order of 0.2−0.3%, i.e., the JLEs work even better for the radii than for the energies. The error is once again largest in ^{16}O, which is expected based on the discussion in Sect. 5.3. For ^{40,48}Ca, the values shrink significantly, but the error for ^{132}Sn is comparable to that of ^{16}O. The most likely explanation is that the situation is analogous to what we found in Fig. 11, and that the radius of ^{132}Sn is not sufficiently well converged—radii generally have a slower convergence in the basis size $e_{\max}$ than energies (see, e.g., [6]). Even so, Fig. 12 shows that the (mean) relative errors caused by applying JLEs to the evaluation of nuclear radii are negligible compared to other sources of error.

6 Conclusions

In the present work, we have initiated a program to explore the use of modewise Johnson–Lindenstrauss embeddings (JLEs) as a compression tool for nuclear many-body theory. Applying such embeddings to the calculation of ground-state energies in second-order Many-Body Perturbation Theory (MBPT(2)), we were able to compress the Hamiltonian in a large-basis calculation more than thousand-fold while only incurring errors below 1%, and we found that the mean relative errors caused by the JLE behave very regularly across single-particle basis sizes and the angular momentum channels of our J-scheme calculations.

The memory savings we achieved through JLE-based compression are comparable to those of an a priori, theory-based selection of Hamiltonian tensor entries that can contribute to the second-order energy and first-order wave function. This means that despite its randomized and therefore data-oblivious nature, the JLE captures the relevant physics with very high accuracy without prior assumptions about the structure of the Hamiltonian or the occupancy of the orbitals in all the nuclei we studied here. We also stress that the compressed Hamiltonian can be readily reused in future many-body applications, although the embedding errors will have to be reassessed if it serves as input for methods other than MBPT(2).

An obvious next step is to apply the JLEs in third and higher orders of MBPT, where the compression of the Hamiltonian will also enable order-of-magnitude reductions in computing time as an additional benefit. Since higher-order energy and wave-function corrections probe all elements of the Hamiltonian, we anticipate somewhat larger errors for any given compression than in MBPT(2). However, the contributions of these corrections to the ground-state energy and other observables get progressively smaller if the many-body perturbation series converges, which will counteract the growing compression error. We already saw examples of this behavior in the present work: The mean relative error of the total ground-state energy E is smaller than that of the second order correction $E^{(2)}$, which is an $O(10\%)$ correction, and the third order correction is typically of order $O(1\%)$. Similarly, the leading correction for the two-body radius operator has a much greater compression error than the energy, but it is a negligible correction to the total radius expectation value and therefore the error does not matter.

Eventually, we intend to apply the JLE in nonperturba-

tive approaches like the In-Medium Similarity Renormalization Group or the Coupled Cluster method, as well as their extensions to open-shell systems and excited states. The working equations of these methods consist of expressions with similar complexity as third (and possibly higher) order MBPT, that must be evaluated iteratively. Moreover, a push towards greater precision in all of these perturbative and non-perturbative techniques will force us to manipulate three-body operators, i.e., mode-six tensors. JLEs will enable crucial computing time and storage savings for such applications.

In parallel to pursuing applications of JLEs in more sophisticated many-body approaches, we will deploy them in M-scheme calculations with symmetry unrestricted single-particle bases that are relevant for the description of nuclei with complex intrinsic structures. For such bases, the dimension for each tensor index is at least an order of magnitude larger than in the J-scheme case discussed in the present work (cf. Sect. 5.1.1). Naively, this should allow us to apply more agressive compression schemes based on our observations for growing $e_{\max}$ in Sect. 4. The relevant tensors will also be sparser due to additional selection rules being in effect, hence we must assess the performance of the random sampling performed by the JLEs under these conditions. Moreover, the M-scheme calculations will typically yield many-body wave functions with broken symmetries that need to be restored explicitly to make accurate comparisons with experimental data (see, e.g., [62–67] and references therein). Since symmetry restoration techniques rely on a delicate balance of interaction and wave function contributions, we will have to carefully study their interplay with the JLEs. To properly deal with all these aspects of future M-scheme applications we might have to design JLE schemes that incorporate features of the underlying physics more explicitly.

Last but not least, we will explore the use of JLEs in the recently launched efforts to factorize nuclear interaction tensors and many-body methods in order to control their computational scaling. The essential numerical steps are typically cast in the form of large-scale optimization problems that are solved with alternating least-squares methods [19,20,28,29], and dimensional reduction via modewise JLEs enables order-of-magnitude speedups in such calculations [38,39,41], in particular when we need to work with explicit three-body operators.

Acknowledgements C. A. Haselby and M. Iwen were supported in part by the National Science Foundation under Award No. DMS 2106472. H. Hergert and R. Wirth acknowledge support by the U.S. Department of Energy, Office of Science, Office of Nuclear Physics under Awards No. DE-SC0017887 and DE-SC0018083 (NUCLEI SciDAC-4 Collaboration.)

Data Availability Statement This manuscript has associated data in a data repository. [Authors' comment: The simulation codes and data for ^{132}Sn obtained with the EM1.8/2.0 interaction in an $e_{\max} = 6$ basis can be accessed in a Github repository at https://github.com/azarerepo/JL4MBPT. Data for other nuclei and basis sizes are available from the authors upon request.]

Appendix A: Additional results

For completeness, we compile detailed results for energy corrections in additional nuclei in this appendix.

Figure 13 shows the angular-momentum channel breakdown of the mean relative error of $E^{(2)}$ for different basis sizes in the nuclei ^{40,48}Ca. The observed trends match what we found and discussed for ^{16}O and ^{132}Sn via Fig. 6.

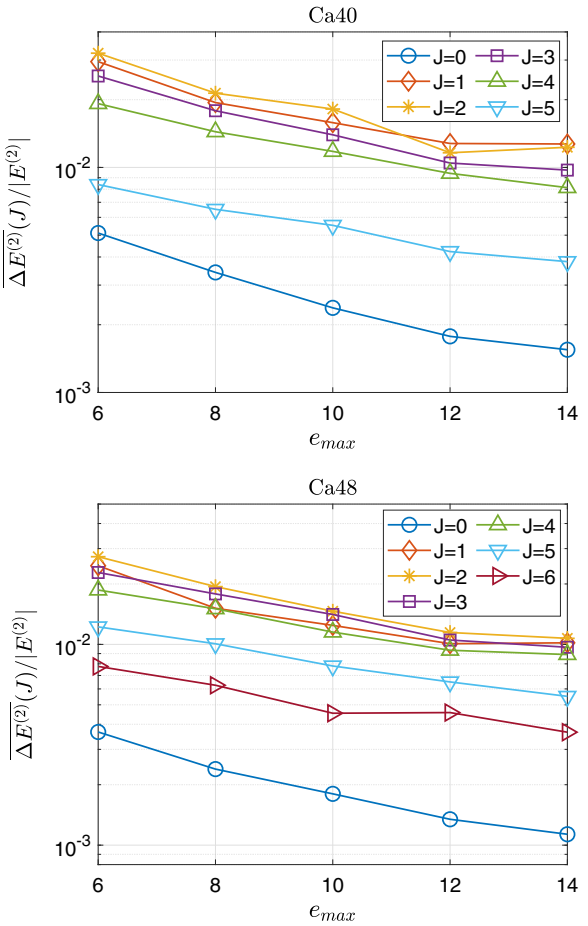

Fig. 13 Contributions of each angular momentum channel to the mean relative error $\overline{\Delta E^{(2)}}/|E^{(2)}$ as a function of $e_{\max}$, for fixed compression $c_{\text{tot}} \leq 10^{-3}$. All calculations were performed with the EM1.8/2.0 interaction. Our favored two-stage JL embedding (RFD + RFD)$_{\text{real}}$ (cf. Sect. 5.2) was used for compression, and 200 trials were carried out

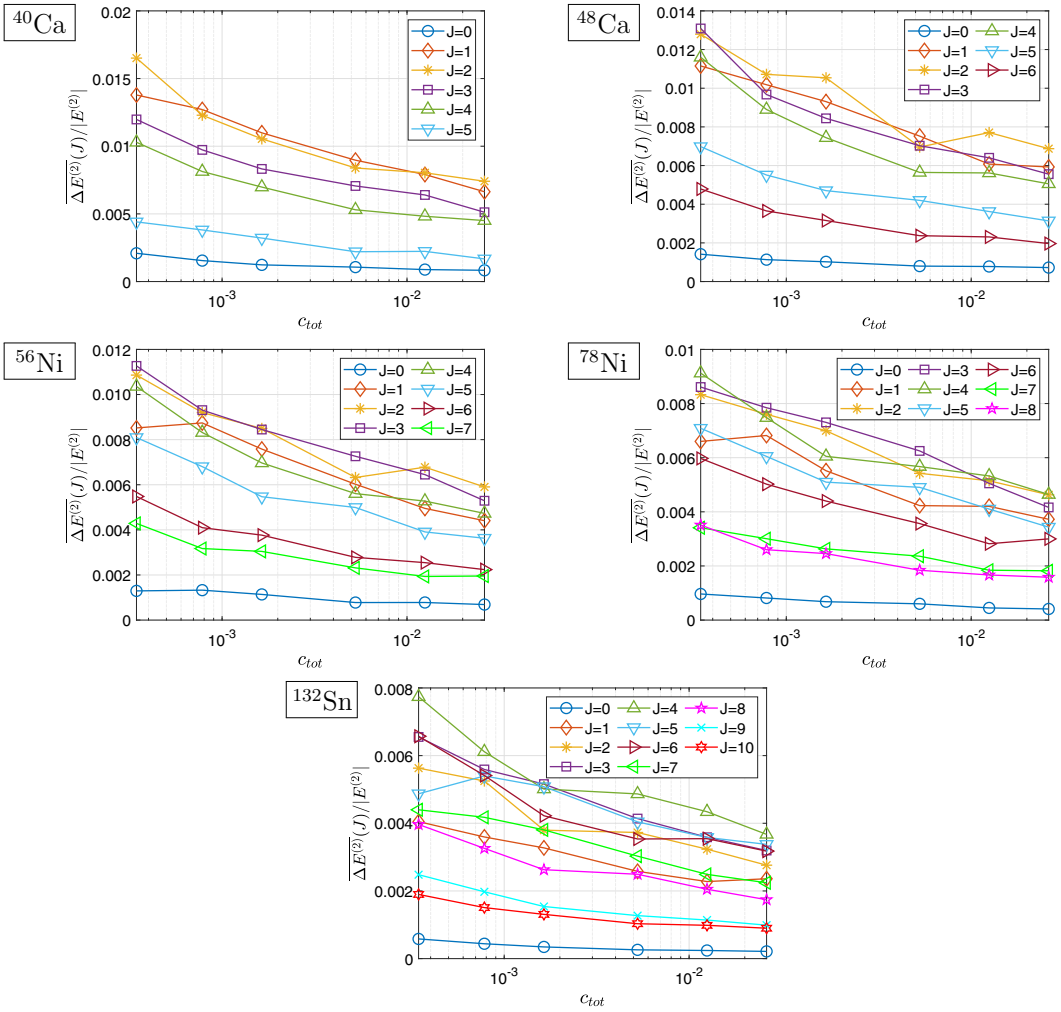

Fig. 14 Contributions of each angular momentum channel to the mean relative error $\overline{\Delta E^{(2)}}/|E^{(2)}|$ as a function of the compression c_{tot}. Calculations were performedwith the EM1.8/2.0 interaction in an $e_{\max} = 14$ basis, and a two-stage JL embedding (RFD + RFD)$_{\text{real}}$ with $c_2 = 0.2$ has been used. 200 trials were performed

Figure 14 extends the results for $\overline{\Delta E^{(2)}}(J)/|E^{(2)}|$ of Fig. 7 for nuclei beyond ^{16}O. The mean relative errors grow exponentially as we decrease c_{tot} over a wide range, with some allowance for fluctuations due to the random sampling performed by the JLE (cf. Sect. 5.3.2).

References

1. B.R. Barrett, P. Navrátil, J.P. Vary, Prog. Part. Nucl. Phys. **69**, 131 (2013). https://doi.org/10.1016/j.ppnp.2012.10.003
2. P. Navrátil, S. Quaglioni, G. Hupin, C. Romero-Redondo, A. Calci, Phys. Scripta **91**(5), 053002 (2016). https://doi.org/10.1088/0031-8949/91/5/053002
3. C. Yang, H.M. Aktulga, P. Maris, E. Ng, J.P. Vary, in *Proceedings of International Conference 'Nuclear Theory in the Supercomputing Era — 2013' (NTSE-2013)*, Ames, 2013, ed. by A.M. Shirokov, A.I. Mazur p. 272
4. H. Hergert, Front. Phys. **8**, 379 (2020). https://doi.org/10.3389/fphy.2020.00379
5. A.B. Balantekin, J. Carlson, D.J. Dean, G.M. Fuller, R.J. Furnstahl, M. Hjorth-Jensen, R.V.F. Janssens, B.A. Li, W. Nazarewicz, F.M. Nunes, W.E. Ormand, S. Reddy, B.M. Sherrill, Mod. Phys. Lett. A **29**(11), 1430010 (2014). https://doi.org/10.1142/S0217732314300109
6. H. Hergert, S.K. Bogner, T.D. Morris, A. Schwenk, K. Tsukiyama, Physics Reports **621**, 165 (2016). https://doi.org/10.1016/j.physrep.2015.12.007
7. H. Hergert, Phys. Scripta **92**(2), 023002 (2017). http://stacks.iop.org/1402-4896/92/i=2/a=023002

8. S.R. Stroberg, H. Hergert, S.K. Bogner, J.D. Holt, Ann. Rev. Nucl. Part. Sci. **69**(1), 307 (2019). https://doi.org/10.1146/annurev-nucl-101917-021120
9. I. Shavitt, R.J. Bartlett, *Many-Body Methods in Chemistry and Physics: MBPT and Coupled-Cluster Theory* (Cambridge University Press, Cambridge, 2009)
10. G. Hagen, T. Papenbrock, M. Hjorth-Jensen, D.J. Dean, Rept. Prog. Phys. **77**(9), 096302 (2014). http://stacks.iop.org/0034-4885/77/i=9/a=096302
11. V. Somà, Front. Phys. **8**, 340 (2020). https://doi.org/10.3389/fphy.2020.00340
12. C. Barbieri, T. Duguet, V. Somà, Phys. Rev. C **105**, 044330 (2022). https://doi.org/10.1103/PhysRevC.105.044330
13. A. Rios, Front. Phys. **8**, 387 (2020). https://doi.org/10.3389/fphy.2020.00387
14. S.R. Stroberg, J.D. Holt, A. Schwenk, J. Simonis, Phys. Rev. Lett. **126**, 022501 (2021). https://doi.org/10.1103/PhysRevLett.126.022501
15. B. Hu, W. Jiang, T. Miyagi, Z. Sun, A. Ekström, C. Forssén, G. Hagen, J.D. Holt, T. Papenbrock, S.R. Stroberg, I. Vernon, Nat. Phys. (2022). https://doi.org/10.1038/s41567-022-01715-8
16. P. Navrátil, G.P. Kamuntavicius, B.R. Barrett, Phys. Rev. C **61**, 044001 (2000)
17. A. Nogga, P. Navrátil, B.R. Barrett, J.P. Vary, Phys. Rev. C **73**, 064002 (2006). https://doi.org/10.1103/PhysRevC.73.064002
18. A. Nogga, H. Kamada, W. Gloeckle, Phys. Rev. Lett. **85**, 944 (2000)
19. R. Schutski, J. Zhao, T.M. Henderson, G.E. Scuseria, J. Chem. Phys. **147**(18), 184113 (2017). https://doi.org/10.1063/1.4996988
20. R.M. Parrish, Y. Zhao, E.G. Hohenstein, T.J. Martínez, J. Chem. Phys. **150**(16), 164118 (2019). https://doi.org/10.1063/1.5092505
21. E.G. Hohenstein, Y. Zhao, R.M. Parrish, T.J. Martínez, J. Chem. Phys. **151**(16), 164121 (2019). https://doi.org/10.1063/1.5121867
22. E.G. Hohenstein, B.S. Fales, R.M. Parrish, T.J. Martínez, J. Chem. Phys. **156**(5), 054102 (2022). https://doi.org/10.1063/5.0077770
23. M. Lesiuk, J. Comput. Chem. **40**(12), 1319 (2019). https://doi.org/10.1002/jcc.25788
24. M. Lesiuk, J. Chem. Theory Comput. **16**(1), 453 (2020). https://doi.org/10.1021/acs.jctc.9b00985
25. M. Lesiuk, J. Chem. Theory Comput. **17**(12), 7632 (2021). https://doi.org/10.1021/acs.jctc.1c00933
26. B. Zhu, R. Wirth, H. Hergert, Phys. Rev. C **104**, 044002 (2021). https://doi.org/10.1103/PhysRevC.104.044002
27. A. Tichai, P. Arthuis, K. Hebeler, M. Heinz, J. Hoppe, A. Schwenk, Phys. Lett. B **821**, 136623 (2021). https://doi.org/10.1016/j.physletb.2021.136623
28. A. Tichai, R. Schutski, G.E. Scuseria, T. Duguet, Phys. Rev. C **99**, 034320 (2019). https://doi.org/10.1103/PhysRevC.99.034320
29. A. Tichai, P. Arthuis, K. Hebeler, M. Heinz, J. Hoppe, A. Schwenk, L. Zurek, Phys. Rev. C **106**, 024320 (2022). https://doi.org/10.1103/PhysRevC.106.024320
30. B. Nagy, F. Jensen, Rev. Comput. Chem. **30**, 93 (2017). https://doi.org/10.1002/9781119356059.ch3
31. A. Tichai, J. Müller, K. Vobig, R. Roth, Phys. Rev. C **99**, 034321 (2019). https://doi.org/10.1103/PhysRevC.99.034321
32. J. Hoppe, A. Tichai, M. Heinz, K. Hebeler, A. Schwenk, Phys. Rev. C **103**, 014321 (2021). https://doi.org/10.1103/PhysRevC.103.014321
33. S.J. Novario, G. Hagen, G.R. Jansen, T. Papenbrock, Phys. Rev. C **102**, 051303 (2020). https://doi.org/10.1103/PhysRevC.102.051303
34. W.B. Johnson, J. Lindenstrauss, in *Conference in modern analysis and probability*, ed. by R. Beals, A. Beck, A.a.o. Bellow. no. 26 in Contemporary Mathematics, 1984 (Conn., New Haven, 1982), p. 189. https://doi.org/10.1090/conm/026/737400
35. N. Halko, P. Martinsson, J. Tropp, SIAM Rev. **53**(2), 217 (2011). https://doi.org/10.1137/090771806
36. M.W. Mahoney, Found. Trends Mach. Learn. **3**(2), 123 (2011). https://doi.org/10.1561/2200000035
37. D.P. Woodruff, Found. Trends Theor. Comput. Sci. **10**(1–2), 1 (2014). https://doi.org/10.1561/0400000060
38. C. Battaglino, G. Ballard, T.G. Kolda, SIAM J. Matrix Anal. Appl. **39**(2), 876 (2018). https://doi.org/10.1137/17M1112303
39. Y. Sun, Y. Guo, C. Luo, J.A. Tropp, M. Udell, SIAM J. Math. Data Sci. (SIMODS) **2**(4), 1123 (2020). https://doi.org/10.1137/19M1257718
40. T.G. Kolda, B.W. Bader, SIAM Rev. **51**(3), 455 (2009). https://doi.org/10.1137/07070111X
41. M.A. Iwen, D. Needell, E. Rebrova, A. Zare, SIAM J. Matrix Anal. Appl. **42**(1), 376 (2021). https://doi.org/10.1137/19M1308116
42. D. Achlioptas, J. Comput. Syst. Sci. **66**(4), 671 (2003)
43. S. Dasgupta, A. Gupta, Random Struct. Algorithms **22**(1), 60 (2003)
44. J. Håstad, J. Algorithms **11**(4), 644 (1990). https://doi.org/10.1016/0196-6774(90)90014-6
45. R. Vershynin, *High-Dimensional Probability: An Introduction with Applications in Data Science. Cambridge Series in Statistical and Probabilistic Mathematics* (Cambridge University Press, 2018)
46. J. Langhammer, R. Roth, C. Stumpf, Phys. Rev. C **86**, 054315 (2012). https://doi.org/10.1103/PhysRevC.86.054315
47. A. Tichai, J. Langhammer, S. Binder, R. Roth, Phys. Lett. B **756**, 283 (2016). https://doi.org/10.1016/j.physletb.2016.03.029
48. A. Tichai, R. Roth, T. Duguet, Front. Phys. **8**, 164 (2020). https://doi.org/10.3389/fphy.2020.00164
49. W. Kutzelnigg, D. Mukherjee, J. Chem. Phys. **107**(2), 432 (1997). https://doi.org/10.1063/1.474405
50. S.B. Khadkikar, V.B. Kamble, Nucl. Phys. A **225**, 352 (1974)
51. H. Hergert, R. Roth, Phys. Lett. B **682**, 27 (2009). https://doi.org/10.1016/j.physletb.2009.10.100
52. G. Hagen, T. Papenbrock, D.J. Dean, A. Schwenk, A. Nogga, M. Włoch, P. Piecuch, Phys. Rev. C **76**, 034302 (2007). https://doi.org/10.1103/PhysRevC.76.034302
53. R. Roth, S. Binder, K. Vobig, A. Calci, J. Langhammer, P. Navrátil, Phys. Rev. Lett. **109**, 052501 (2012). https://doi.org/10.1103/PhysRevLett.109.052501
54. A. Tichai, R. Wirth, J. Ripoche, T. Duguet, Eur. Phys. J. A **56**(10), 272 (2020). https://doi.org/10.1140/epja/s10050-020-00233-6
55. K. Hebeler, S.K. Bogner, R.J. Furnstahl, A. Nogga, A. Schwenk, Phys. Rev. C **83**, 031301 (2011). https://doi.org/10.1103/PhysRevC.83.031301
56. A. Nogga, S.K. Bogner, A. Schwenk, Phys. Rev. C **70**, 061002 (2004). https://doi.org/10.1103/PhysRevC.70.061002
57. S.K. Bogner, R.J. Furnstahl, A. Schwenk, Prog. Part. Nucl. Phys. **65**, 94 (2010). https://doi.org/10.1016/j.ppnp.2010.03.001
58. T. Miyagi, S.R. Stroberg, P. Navrátil, K. Hebeler, J.D. Holt, Phys. Rev. C **105**, 014302 (2022). https://doi.org/10.1103/PhysRevC.105.014302
59. K. Hebeler, V. Durant, J. Hoppe, M. Heinz, A. Schwenk, J. Simonis, A. Tichai, Phys. Rev. C **107**, 024310 (2023), https://doi.org/10.1103/PhysRevC.107.024310
60. E. Gebrerufael, A. Calci, R. Roth, Phys. Rev. C **93**, 031301 (2016). https://doi.org/10.1103/PhysRevC.93.031301
61. F. Krahmer, R. Ward, SIAM J. Math. Anal. **43**(3), 1269 (2011)
62. J.M. Yao, *Symmetry Restoration Methods* (Springer Nature Singapore, Singapore, 2022), pp. 1–36. https://doi.org/10.1007/978-981-15-8818-1_18-1
63. J.M. Yao, B. Bally, J. Engel, R. Wirth, T.R. Rodríguez, H. Hergert, Phys. Rev. Lett. **124**, 232501 (2020). https://doi.org/10.1103/PhysRevLett.124.232501
64. M. Frosini, T. Duguet, J.P. Ebran, V. Somà, Eur. Phys. J. A **58**(4) (2022). https://doi.org/10.1140/epja/s10050-022-00692-z

65. M. Frosini, T. Duguet, J.P. Ebran, B. Bally, H. Hergert, T.R. Rodríguez, R. Roth, J.M. Yao, V. Somà, Eur. Phys. J. A **58**(4), 64 (2022). https://doi.org/10.1140/epja/s10050-022-00694-x
66. M. Frosini, T. Duguet, J.P. Ebran, B. Bally, T. Mongelli, T.R. Rodríguez, R. Roth, V. Somà, Eur. Phys. J. A **58**(4) (2022). https://doi.org/10.1140/epja/s10050-022-00693-y
67. G. Hagen, S.J. Novario, Z.H. Sun, T. Papenbrock, G.R. Jansen, J.G. Lietz, T. Duguet, A. Tichai, Phys. Rev. C **105**, 064311 (2022). https://doi.org/10.1103/PhysRevC.105.064311